

ALMA Observations of Young Eruptive Stars: continuum disk sizes and molecular outflows

ANTONIO S. HALES,^{1,2} SEBASTIÁN PÉREZ,³ CAMILO GONZALEZ-RUILOVA,^{4,5} LUCAS A. CIEZA,⁵ JONATHAN P. WILLIAMS,⁶
PATRICK D. SHEEHAN,² CRISTIÁN LÓPEZ,¹ SIMON CASASSUS,⁴ DAVID A. PRINCIPE,⁷ AND ALICE ZURLO^{8,5}

¹Joint ALMA Observatory, Avenida Alonso de Córdova 3107, Vitacura 7630355, Santiago, Chile

²National Radio Astronomy Observatory, 520 Edgemont Road, Charlottesville, VA 22903-2475, United States of America

³Departamento de Física, Universidad de Santiago de Chile, Av. Ecuador 3493, Estación Central, Santiago, Chile

⁴Departamento de Astronomía, Universidad de Chile, Casilla 36-D, Santiago 8330015, Chile

⁵Núcleo de Astronomía, Facultad de Ingeniería y Ciencias, Universidad Diego Portales, Av. Ejercito 441, Santiago, Chile

⁶Institute for Astronomy, University of Hawaii, Honolulu, HI 96822, USA

⁷MIT Kavli Institute of Astrophysics and Space Research, 70 Vassar St. Cambridge, MA, 02139, USA

⁸Escuela de Ingeniería Industrial, Facultad de Ingeniería y Ciencias, Universidad Diego Portales, Av. Ejercito 441, Santiago, Chile

ABSTRACT

We present Atacama Large Millimeter/submillimeter Array (ALMA) 1.3 mm observations of four young, eruptive star-disk systems at $0''.4$ resolution: two FUors (V582 Aur and V900 Mon), one EXor (UZ Tau E) and one source with an ambiguous FU/EXor classification (GM Cha). The disks around GM Cha, V900 Mon and UZ Tau E are resolved. These observations increase the sample of FU/EXors observed at sub-arcsecond resolution by 15%. The disk sizes and masses of FU/EXors objects observed by ALMA so far suggest that FUor disks are more massive than Class 0/I disks in Orion and Class II disks in Lupus of similar size. EXor disks in contrast do not seem to be distinguishable from these two populations. We reach similar conclusions when comparing the FU/EXor sample to the Class I and Class II disks in Ophiuchus. FUor disks around binaries are host to more compact disks than those in single-star systems, similar to non-eruptive young disks. We detect a wide-angle outflow around GM Cha in ^{12}CO emission, wider than typical Class I objects and more similar to those found around some FUor objects. We use radiative transfer models to fit the continuum and line data of the well-studied disk around UZ Tau E. The line data is well described by a keplerian disk, with no evidence of outflow activity (similar to other EXors). The detection of wide-angle outflows in FUors and not in EXors support to the current picture in which FUors are more likely to represent an accretion burst in the protostellar phase (Class I), while EXors are smaller accretion events in the protoplanetary (Class II) phase.

Keywords: protoplanetary disks – stars: formation – stars: evolution – stars: individual (GM Cha, UZ Tau E, V582 Aur, V900 Mon) – stars: pre-main sequence – accretion

1. INTRODUCTION

Multi-epoch accretion outbursts are believed to play a key role in the build-up of the final stellar mass (Hartmann 2008; Hartmann et al. 2016). Episodes of variable accretion are invoked to solve the well-known luminosity problem, in which low-mass stars appear fainter than predictions of steady-state accretion models (Kenyon et al. 1990; Evans et al. 2009). Despite being key to our understanding of low-mass star (and planet) formation, the exact mechanisms that trigger outbursts are still poorly understood, and this topic is of growing interest as observational capabilities at long wavelengths (such as ALMA) have developed (see Audard et al. 2014, for a review).

Outbursting sources have been divided into two classes, FUors and EXors (named after prototypes FU Ori and EX Lupi respectively). FUors have large ($\Delta V_{\text{mag}} \sim 5$), long-lived (years to decades) outbursts (Herbig 1966), whereas EXors have moderate ($\Delta V_{\text{mag}} \sim 2-4$), shorter (days/months) episodes of high accretion. Several observational signatures indicate differences in physical structures and accretion processes of each class, which suggest that FUors and EXors might correspond to different evolutionary stages.

EXors show rich optical and infrared emission lines similar to those of classical T Tauri stars (CTTS), which brighten during the burst, consistent with magnetospheric accretion. They also have spectral energy distributions (SEDs) similar to those of Class II sources (e.g. Sipos et al. 2009), suggesting these are typical star+disk systems with no detectable remnant envelope. The few available optical spectra of FUors in quiet states show they also resemble those of CTTS (Herbig, & Harlan 1971). In outburst, however, FUors show little signs of magnetospheric accretion and instead exhibit optical

P-cygni profiles at H α and sodium lines (indicative of strong winds of $\sim 10\%$ the accretion rate; Calvet et al. 1993), as well as double peaked absorption features in some optical and near-IR lines. The extremely high luminosity and spectroscopic features of the prototype FU Orionis itself have been explained in the frame of an accretion disk model in which the disk is internally heated through strong viscous accretion, overwhelming the stellar photosphere (Hartmann, & Kenyon 1985; Hartmann & Kenyon 1996). This explains the high accretion rates and double, differential, absorption lines (with the difference in line profiles explained by absorption at different radii, e.g. Zhu et al. 2009a). Most FUors are also associated with reflection nebulae, and many have Class I SEDs with prominent CO outflows observed at millimeter wavelengths, both indicating that they are still partially surrounded by their parent envelope and therefore suggesting a younger evolutionary stage compared to EXors (see Reipurth, & Aspin 2010; Hartmann et al. 2016, for review). Objects that share the spectroscopic features of FUors, but for which outbursts have never been observed are called FUor-like objects (see Connelley & Reipurth 2018, for details).

Different mechanisms have been proposed to explain the origin for the outbursts (Audard et al. 2014): disk fragmentation plus subsequent inward migration of clumps (Vorobyov & Basu 2015), a combination of magnetorotational and gravitational instabilities (Armitage et al. 2001), and enhanced accretion induced by stellar (Bonnell & Bastien 1992) or planetary companions (Lodato & Clarke 2004). The key ingredients to distinguish between the above outburst mechanisms are the total disk mass and the disk spatial structure. However, only a few FU/EXor objects have been recently observed at sufficient angular resolution at millimeter/submillimeter wavelengths. Recent surveys with ALMA and the SMA (Cieza et al. 2018; Liu et al. 2018) have shown that 1.3 mm fluxes of the outbursting sources span over three orders of magnitude, but the FUor objects are significantly brighter than the EXor objects and typical Class II disks.

The inferred disk masses for the brightest FUor objects are large enough that they may be gravitationally unstable. Nevertheless, follow up observations at $0''.03$ (12 au) resolution of V883 Ori, the most massive disk in the survey, were unable to identify the predicted signatures of instabilities or fragmentation (e.g. spirals or clumps). The fainter targets are all EXor objects and have low disk masses, $\sim 1-5 M_{\text{Jup}}$, that imply gravitational instability is unlikely to play a role in their outbursts (e.g., Cieza et al. 2018).

Some FUor objects are close binaries with both components hosting disks (e.g. FU Orionis, L1551 IRS, HBC 494; Hales et al. 2015; Cruz-Sáenz de Miera et al. 2019; Zurlo et al. in prep.), whose interaction could help explain the outbursts in some of the systems. Recent ALMA observations of FU Orionis show that the disks are indeed compact in continuum emission (11 au in radius) while the gas kinematics displays extended features possibly tracing binary and/or intra-cloud interactions (Pérez et al. 2020).

ALMA spectral line observations of ^{12}CO show that FUors have active circumstellar environments characterized

by strong outflows interacting with larger-scale structure (Ruíz-Rodríguez et al. 2017a; Ruíz-Rodríguez et al. 2017b; Zurlo et al. 2017; Kóspál et al. 2017b; Principe et al. 2018; Takami et al. 2019). On the other hand, EXor sources do not show detectable outflows, with the possible exception of V1647 Ori, a system with an unclear FUor/EXor classification (Principe et al. 2018) and EX Lupi itself (around which a small arc-shaped feature is detected at $\sim 2 \text{ km s}^{-1}$ from the systemic velocity; Hales et al. 2018). Although the number of observed sources is small, the differences in outflow activity between FUors and EXors suggest that the two types of objects represent an evolutionary sequence comparable to normal Class I and Class II respectively. V346 Nor has observational properties more similar to Class 0/I protostars, consistent with the growing number of Class 0 sources discovered to show eruptive behavior (Safron et al. 2015; Johnstone et al. 2018). This suggests that episodic accretion may play an important role even at earlier protostellar stages. Studying the larger-scale structure of eruptive sources is thus crucial for understanding the nature of this common, yet short-lived, high mass accretion variability in young stars.

This work aims to contribute a better understanding of the differences between the two classes of young eruptive stars, FUors and EXors, and how their disk masses, sizes and associated gas emission, compare to Class I and Class II protostars. Are FU/EXor disks massive enough to trigger gravitational instability? Do they show the predicted signatures of a gravitationally unstable disk? Are all variable accretion sources associated with large molecular outflows? For this purpose we present ALMA observations of four eruptive sources to characterize their distribution of dust and gas, and to compare them to those of non-eruptive protostars. Section 2 describes our target sample, observations and data reduction. In Section 3 we present our results, which are discussed in Section 4. Section 5 presents our conclusions.

2. SAMPLE SELECTION AND ALMA OBSERVATIONS

2.1. Target Sample

There are about ~ 38 known FUor/EXor objects within $\sim 1 \text{ kpc}$, of which ~ 20 are observable with ALMA (with declination $< +40^\circ$; Audard et al. 2014). So far ~ 14 of them have already been observed by ALMA at moderate angular resolution ($0''.2-0''.9$; Hales et al. 2015; Kóspál et al. 2017b; Cieza et al. 2018; Hales et al. 2018; Takami et al. 2019; Cruz-Sáenz de Miera et al. 2019). In this work we present ALMA Band 6 observations of four FUor/EXor objects observed in ALMA Cycle 5 (project code 2017.1.01031.S, PI Hales). The targets were selected from the list of Audard et al. (2014) and include two FUors (V582 Aur and V900 Mon), one EXor (UZ Tau E) and one source with ambiguous FU/EXor classification (GM Cha). This apparently small sample represents 10% of known FUor/EXor objects, and these observations increase the number of eruptive sources observed at sub-arcsecond resolution by 15% (since two of our targets, V900 Mon and UZ Tau E, have already been observed at similar or higher angular resolution; Takami et al. 2019; Long et al. 2018).

Table 1. Summary of ALMA Observations (this work)

Name	Execution Block	N Ant.	Date	ToS	Avg. Elev.	Mean PWV	Phase RMS	Baseline	AR	MRS
				(sec)	(deg)	(mm)	(rad)	(m)	($''$)	($''$)
V582 Aur	uid://A002/Xd248b5/X4ff9	41	2018-09-22	989	30.3	0.2	0.435	15.1-1397.8	0.3	3.6
V900 Mon	uid://A002/Xd23397/Xe02d	43	2018-09-21	1128	75.4	0.2	0.411	15.1-1397.8	0.3	3.7
UZ Tau	uid://A002/Xd23397/X41f6	47	2018-09-20	1273	31.2	0.4	0.472	15.1-1397.8	0.3	3.8
GM Cha	uid://A002/Xd28a9e/X4a7b	43	2018-09-27	1417	36.4	1.5	0.498	15.1-1397.8	0.3	3.6
GM Cha	uid://A002/Xd29c1f/X5b5e	43	2018-09-29	1445	36.3	1.0	0.458	15.1-1397.8	0.2	3.3

NOTE—Summary of the new ALMA observations presented in this work, including number of antennas, total time on source (ToS), target average elevation, mean precipitable water vapor column (PWV) in the atmosphere, phase RMS measured on the bandpass calibrator, minimum and maximum baseline lengths, expected angular resolution (AR) and maximum recoverable scale (MRS).

Table 2. Summary of continuum disk detections. Disks are sorted by declining disk mass. Object type, Spectral type, and L_{Bol} , and Companions are taken from [Audard et al. \(2014\)](#). Distances are obtained from the second data release (DR2) of Gaia ([Gaia Collaboration et al. 2018](#)), except for GM Cha for which we adopt the distance to Cha I from [Dzib et al. \(2018\)](#).

	V582 Aur	V900 Mon	UZ Tau E	GM Cha
Object type	FUor	FUor	EXor	FU/EXor
$L_{\text{Bol}}(L_{\odot})$	-	106	1.7	>1.5
Companions	-	N	Y (SB+4 $''$)	Y (10 $''$)
$F_{1.3\text{mm}}$ (mJy) ^a	5.3±0.6	9.8±0.1	134±1	10.4±0.1
Major axis (mas) ^b	-	72±11	668±20	613±8
Minor axis (mas) ^b	-	60±20	396±22	221±2
Position angle (deg)	-	164±63	90±4	27.8±0.3
Disk radius (au)	-	54	44	49
Inclination (deg)	-	50	59	70
Distance (pc)	2575	1500	131	192
$M_{\text{dust}}(M_{\oplus})$ for $T = 20\text{ K}$	1055	662	69	11
$M_{\text{dust}}(M_{\oplus})$ for $T = 60\text{ K}$	291	182	19	3
$M_{\text{disk}}(M_{\text{Jup}})$ for $T = 20\text{ K}$	332	208	22	3
Peak (mJy beam $^{-1}$)	4.2	9.4	54.7	5.9
Rms (mJy beam $^{-1}$)	1.41×10^{-1}	5.23×10^{-2}	8.08×10^{-2}	3.56×10^{-2}
Beam Major axis ($''$)	0.49	0.35	0.57	0.57
Beam Minor axis ($''$)	0.28	0.32	0.34	0.37
Beam Position angle (deg)	153.2	77.5	-40.1	17.2

^aUncertainties on the continuum flux do not include the absolute flux uncertainty of ALMA.

^bDeconvolved disk sizes reported by IMFIT.

V900 Mon is an FUor object discovered by [Thommes et al. \(2011\)](#), who reported a brightening of at least 4 magnitudes in optical magnitude, while follow up observations indicate the object shows FUor characteristics such as P-Cygni profiles in $H\alpha$ and sodium lines, CO absorption in near-IR, as well as an association with a bright, compact reflection nebula ([Reipurth et al. 2012](#)). [Takami et al. \(2019\)](#) presented recent ALMA observations that show the presence of a CO outflow and rotating envelope.

V582 Aur is young eruptive system first identified due to an optical brightening of ~ 4 magnitudes that took place sometime between 1982 and 1986, followed by the appear-

ance of a nebula that was not visible in previous optical images ([Samus 2009](#)). [Semkov et al. \(2013\)](#) studied the optical photometry and spectra and showed that the star has spectroscopic signatures typical of FUors, although some of the color changes have similarities with UXor-type stars (UXors are young stars that show stochastic variability that can be explained by eclipses due to dust fragments in their circumstellar disks; [Grinin et al. 2019](#)). [Ábrahám et al. \(2018\)](#) studied the color variations of V582 Aur and suggest that the two 1 yr long dips seen in 2012 and 2017 in the light curve are due to variable extinction rather than enhanced accretion, and therefore more similar to UXors than to FUor/EXors. [Zsidi et](#)

al. (2019) combine optical, near- and mid-infrared photometry to investigate the physical structure of the dust responsible for the dimming. Millimeter observations with IRAM 30m and Northern Extended Millimeter Array (NOEMA) reveal a compact continuum source at the position of V582 Aur, together with other clumps in both continuum and CO isotopologues (Ábrahám et al. 2018).

GM Cha (ISO-Cha I 192) is a Class I/II source located in the Chameleon I dark cloud (Moody, & Stahler 2017; Mottram et al. 2017). The source has no optical counterpart, is located in a region of high extinction (Jones et al. 1985), and is associated with a ^{12}CO outflow (Mattila et al. 1989; Mottram et al. 2017). From 1996 to 1999 the K_S -band magnitude increased by 2 magnitudes (Persi et al. 2007), and there is evidence of possible elongated infrared nebulosity in the direction of the outflow. As with V1647 Ori, the observational characteristics of GM Cha are similar to both FUors and EXors. The SED can be well described by a star+disk+infalling envelope and the presence of a reflection nebula suggests similarities with FUors. However, it shows no $2.3\ \mu\text{m}$ CO band head (neither in absorption or emission), and the derived accretion rate of $10^{-7}\ M_{\odot}\ \text{yr}^{-1}$ is three orders of magnitude lower than those of FUors (Persi et al. 2007).

UZ Tau is a well-studied quadruple system, containing a spectroscopic binary with a separation of ~ 0.03 au (Mathieu et al. 1996) surrounded by a large circumbinary disk (UZ Tau E; Tripathi et al. 2018), and another M3+M3 binary pair with a $0''.34$ (~ 48 au) projected separation (UZ Tau W). UZ Tau E continuum disk was imaged by Long et al. (2018) at $0''.13 \times 0''.11$ resolution and found the presence of at least three sets of rings spanning from 0 to ~ 100 au with one clearly defined gap at 69 au. UZ Tau E shows moderate (~ 1 mag) short-term variability in the optical and infrared, and exhibits characteristics of an EXor (Lorenzetti et al. 2007). Jensen et al. (2007) showed that the periodic variability of UZ Tau E could be explained by variable accretion caused by interactions between the binary orbit and the circumbinary disk. Czekala et al. (2019) used ALMA data of ^{13}CO and C^{18}O to study the degree of alignment of the binary and the circumbinary disk, and determined that the disk and the stars are nearly coplanar, which may imply that planets formed in this system will also be coplanar.

2.2. Observations

ALMA observations of these four targets were acquired between September 20th and September 29th 2018 using the Band 6 receiver (~ 230 GHz). The total number of available 12 meter antennas ranged from 41 to 47, providing baselines ranging from 15.1 m to 1.397 km. A summary of the observations such as precipitable water vapor column (PWV) in the atmosphere, phase RMS, target elevation and time on source (ToS), number of antennas, expected angular resolution (AR) and maximum recoverable scale (MRS) are presented in Table 1. Standard observations of bandpass, flux and phase calibrators were also included.

The spectral setup was chosen to target the $^{12}\text{CO}(2-1)$, $^{13}\text{CO}(2-1)$ and $\text{C}^{18}\text{O}(2-1)$ transitions of carbon monox-

ide (rest frequencies of 230.538 GHz, 220.399 GHz, 219.560 GHz, and 218.437 GHz, respectively). The ALMA correlator was configured in Frequency Division Mode (FDM) to provide spectral resolutions of $0.09\ \text{km}\ \text{s}^{-1}$. Two spectral windows in Time Division Mode (TDM) to image dust continuum were set up at central frequencies of 218.0 GHz and 233.0 GHz, each with total bandwidths of 1.875 GHz.

2.3. Data Reduction

All data were calibrated using the ALMA Science Pipeline (version 40896 Pipeline-CASA51-P2-B) in CASA 5.1 (CASA¹; McMullin et al. 2007) by staff at the North American ALMA Science Center. The Pipeline uses CASA tasks to perform the data reduction and calibration in a standard fashion which includes correction for Water Vapor Radiometer (WVR) and system temperature, as well as bandpass, phase, and amplitude calibrations.

Imaging of the continuum and molecular emission lines was performed using the TCLEAN task in CASA. The two continuum spectral windows were imaged together using Briggs weighting with a robust parameter of 0.5, resulting in a final continuum image centered at 225.5 GHz. The synthesized beam size achieved for each target are shown in Table 2. Since all targets are bright enough for self-calibration, a single iteration of phase-only self-calibration was performed to improve coherence. The resulting continuum sensitivity achieved for each target is shown in Table 2.

Imaging of the spectral lines was performed using TCLEAN on the continuum subtracted data (which subtracted using CASA task UVCNTSUB). Self-calibration tables from the continuum data were applied to the spectral line data before imaging the CO lines. During TCLEANING the spectral channels were binned to $0.3\ \text{km}\ \text{s}^{-1}$ for UZ Tau E and to $0.5\ \text{km}\ \text{s}^{-1}$ for the other sources. TCLEAN was run with natural weighting to enhance sensitivity.

3. RESULTS

3.1. Continuum

All observed targets are detected at a high signal-to-noise ratio in continuum emission (Figure 1). We use the CASA task IMFIT to fit an elliptical Gaussian to the images and derive emitting region sizes (deconvolved from the beam) and dust continuum fluxes. We use these sizes as a proxy for the disk radius. The disk sizes are thus estimated from the deconvolved Gaussian FWHM/2 (see Section 4.1 for a discussion on the reliability of this method for estimating disk sizes). The disks around GM Cha and UZ Tau E are resolved. V900 Mon is marginally resolved, as can be seen by inspecting the visibilities (shown in the right panel of Figure 1). V582 Aur, being significantly more distant, is unresolved. The large circumbinary disk around UZ Tau E is resolved, while the individual disks around each component of

¹ <http://casa.nrao.edu/>

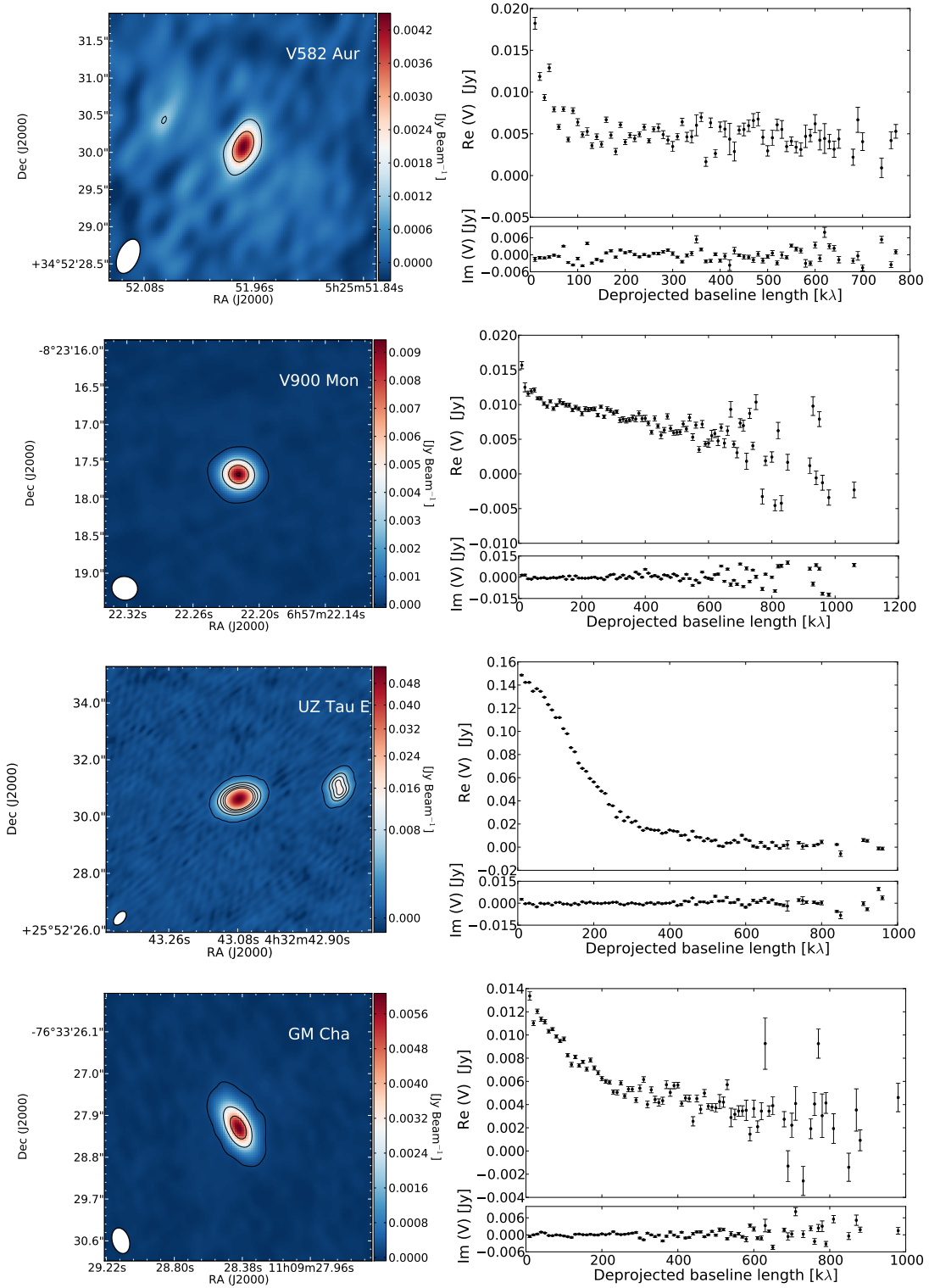


Figure 1. *Left:* ALMA 1.3mm continuum images for the FUor (top) and EXor (bottom) sources. Contour levels for V900 Mon, UZ Tau and GM Cha start at 5σ and increase in steps of 5σ , and in steps of 10σ for V582 Aur. The synthesized beam size achieved for each target are shown in the lower left. *Right:* Averaged continuum visibilities.

UZ Tau W are marginally resolved. The derived disk parameters are presented in Table 2. The inclinations are derived from the ratio of the deconvolved minor and major axes. The 225.5 GHz flux for UZ Tau E is consistent with the CARMA measurement of 131 ± 6 mJy (Tripathi et al. 2018), as well as with 0.12" resolution ALMA observations (129.5 ± 0.2 mJy; Long et al. 2018). The disk radius we derive for V900 Mon (54 au) is consistent with the 45 au value inferred by Takami et al. (2019) with a factor ~ 2 better spatial resolution.

The 1.3 mm photometry of each disk is listed in Table 2. These fluxes will be used to estimate dust masses using the optically thin approximation in Section 4.1 along with a discussion of the key assumptions and their caveats.

3.2. Spectral line data

Spectral line emission ($J = 2-1$) from the three main isotopologues of CO was detected in all sources. Takami et al. (2019) recently presented a study of V900 Mon in similar spectral transitions, and a detailed analysis of the spectral line data for GM Cha will be presented in a separate paper (C. Gonzalez et al. in prep.). Therefore in this work we present the ^{12}CO data for all four sources for comparison purposes, and the complete line data (^{12}CO , ^{13}CO and C^{18}O) only for UZ Tau E and V582 Aur.

Integrated line emission (moment 0) maps for ^{12}CO are shown in Figure 2. The total integrated line emission per molecule for UZ Tau E and V582 Aur are presented in Table 3. The moment maps and the final integrated line fluxes are all computed integrating the channel with emission above $3\text{-}\sigma$, and correspond to the velocity ranges annotated in Figure 2. The spectral profiles for UZ Tau E and V582 Aur (integrated over the circular apertures shown in Figure 2) are shown in Figure 3. Figure 4 show intensity-weighted velocity fields (moment 1) images in ^{12}CO , ^{13}CO and C^{18}O for UZ Tau E. Velocity maps showing each CO isotopologue for V582 Aur are presented in Appendix C, together with moment 0 maps of ^{13}CO and C^{18}O .

All sources show very different morphologies in their ^{12}CO emission. While the UZ Tau E disk shows a clear Keplerian rotation pattern, V900 Mon and more noticeably GM Cha both show conical cavity walls similar to those detected around other FUors (Figure 5). V582 Aur ^{12}CO moment 0 map shows widespread emission and at least three peaks in its spectrum. This is due to its association to a star-forming filamentary cloud with velocities spanning $[-12.5, -7.5]$ km s $^{-1}$ (Dewangan et al. 2018; Ábrahám et al. 2018). The ALMA ^{12}CO data shows compact emission within ~ 1.4 arcsecond (3500 au) from the position of the FUor at velocities between $[-12.85, -11.5]$ km s $^{-1}$ for ^{12}CO , and $[-12.10, -11.5]$ km s $^{-1}$ for ^{13}CO , before cloud contamination becomes dominant (see full channel maps in Appendix C). Central emission near V582 Aur in ^{13}CO and C^{18}O was previously reported (Ábrahám et al. 2018) using NOEMA. Because of its location close to the source and velocities further away from the main cloud velocities, it is possible that this central emission is associated to the FUor.

4. DISCUSSION

4.1. Disk Masses

A crude estimation of the disk dust masses can be obtained under the standard assumption that the continuum emission from disks is optically thin at millimeter wavelengths (e.g. Hildebrand 1983). This is certainly not true in the disk inner regions (usually in the inner 5-10 au), but it is considered to be a reasonable assumption for the rest of the disk (e.g., Cieza et al. 2018).

We estimate the disk dust masses from the optically thin assumption that relates the observed flux, F_ν , to the mass of solids (e.g. Beckwith et al. 1990), via

$$M_{\text{dust}} = \frac{F_\nu d^2}{\kappa_\nu B_\nu(T)}, \quad (1)$$

where B_ν is the Planck function for a given temperature T , κ_ν is the dust opacity and d is the distance to the emitting dust. We note that, at millimeter frequencies, the low temperatures of some disks (<100 K) imply that the Rayleigh-Jeans regime is not ideal for approximating the Planck function. For example, at $T=20$ K and $\nu=225$ GHz, there is a 30% difference between calculating the full Planck function and the Rayleigh-Jeans approximation. Therefore, caution must be taken when employing the linear temperature dependence offered by Rayleigh-Jeans.

As discussed in Cieza et al. (2018), the assumption of optically thin emission will underestimate the total dust mass, while the assumption of a temperature of 20 K may overestimate the mass if the dust is warmer, therefore the two effects may partially offset each other (since the total mass approximately scales as the inverse of temperature). To which extent this statement is valid may depend on the properties of each object. For instance, since FUor sources can be ~ 100 times more luminous than normal stars in Class II disks, one would expect the average temperature of disks in FUor sources to be a factor of ~ 3 higher than in normal Class II disks (since the disk temperature scales with the stellar luminosity $T \propto L^{1/4}$; Chiang & Goldreich 1997). This will result in an overestimation of the disk mass by a similar amount. On the other hand, the more massive and/or compact become very optically thick in their inner regions and therefore the optically thin assumption will underestimate the total dust mass (e.g. Liu et al. 2019). In the case of V833 Ori, Cieza et al. (2018) found that the total dust mass obtained using the optically thin approximation is similar to the mass derived using radiative transfer which takes into account the high optical depth in the disk inner regions. However, for HBC 494 and V2775 Ori, they found that the assumption of optically thin emission and 20 K dust temperature overestimate the mass by a factor of ~ 2 when compared to the radiative transfer results. This can be attributed to the fact that the disks around HBC 494 and V2775 Ori are more compact than the disk around V833 Ori, and therefore the average disk temperatures are likely higher than 20 K. This highlights the need for combining resolved images with radiative transfer techniques in order to infer the true properties of these disks.

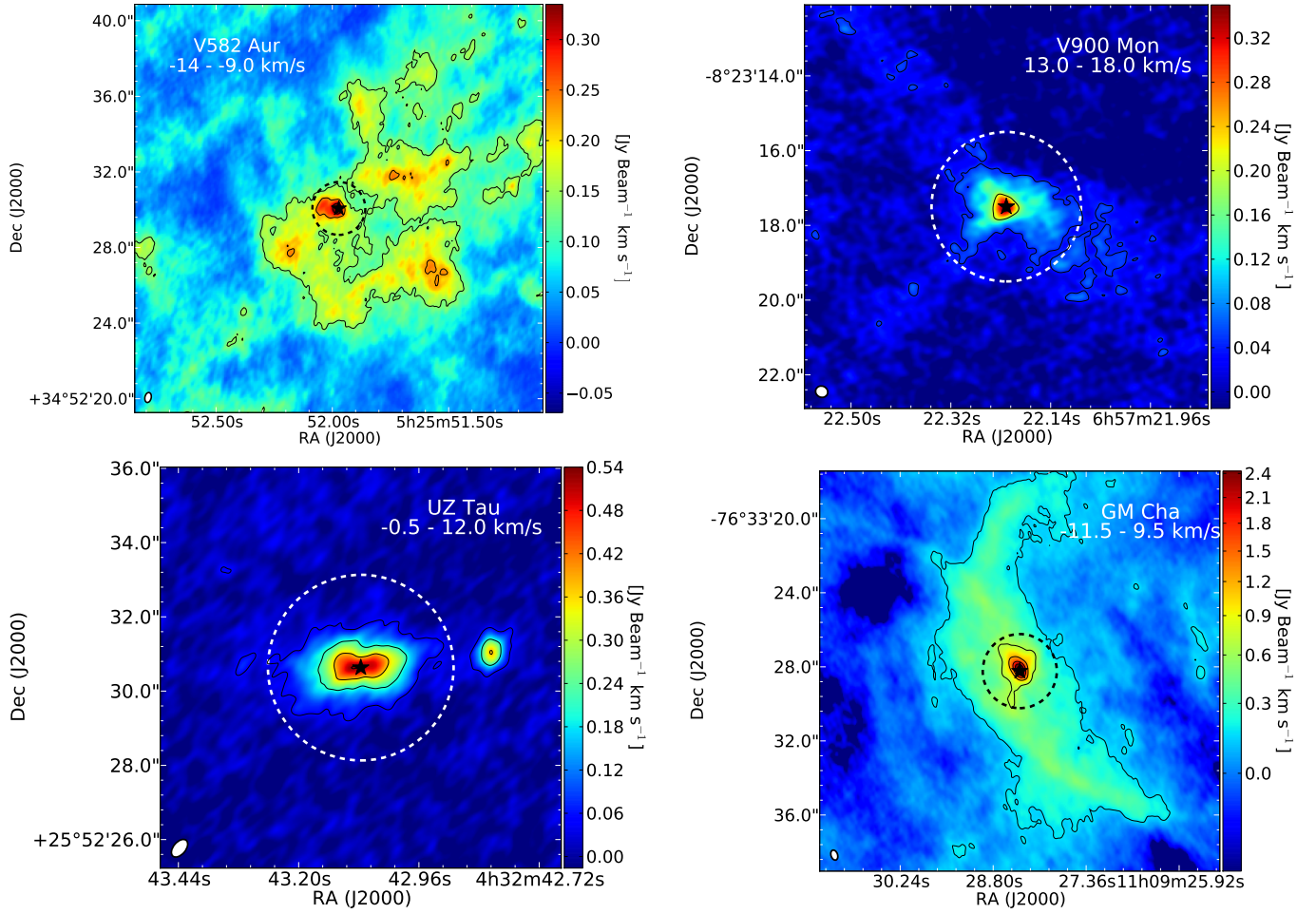


Figure 2. ^{12}CO integrated intensity maps (moment 0) for all targets. The dashed circles shows the region used to compute the integrated line emissions listed in Table 3. The peak position of the continuum is shown with a star.

Table 3. Measured CO J=2-1 Integrated Fluxes (angular integrated intensity)

Source	^{12}CO	^{13}CO	C^{18}O
UZ Tau	7.02 ± 0.02	1.16 ± 0.02	0.42 ± 0.01
V582 Aur	5.51 ± 0.09	2.83 ± 0.07	0.81 ± 0.035
V900 Mon	5.06 ± 0.02	3.77 ± 0.02	1.65 ± 0.02
GM Cha	36.03 ± 0.04	3.67 ± 0.02	0.52 ± 0.01

NOTE—Integrated line fluxes are in units of mJy km s^{-1} . Errors do not include the absolute flux uncertainty which is estimated to be between 7 and 10% in Band 6.

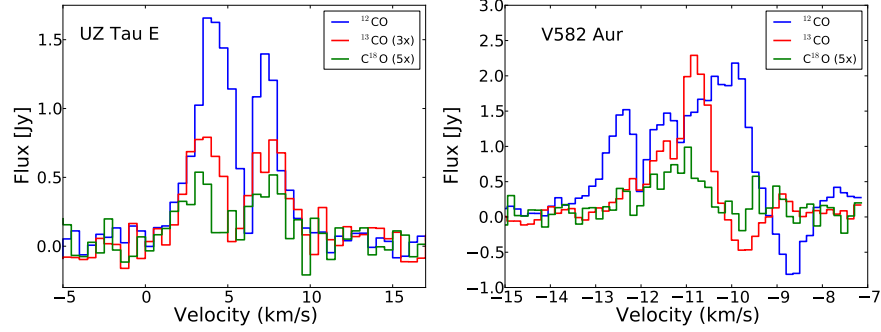


Figure 3. Integrated spectra for UZ Tau E and V582 Aur in ^{12}CO , ^{13}CO and C^{18}O . The integrated line profiles were computed by integrating the emission in the regions corresponding to the dotted circles in Figure 2. The spectra may have been scaled for display purposes, as specified in each figure.

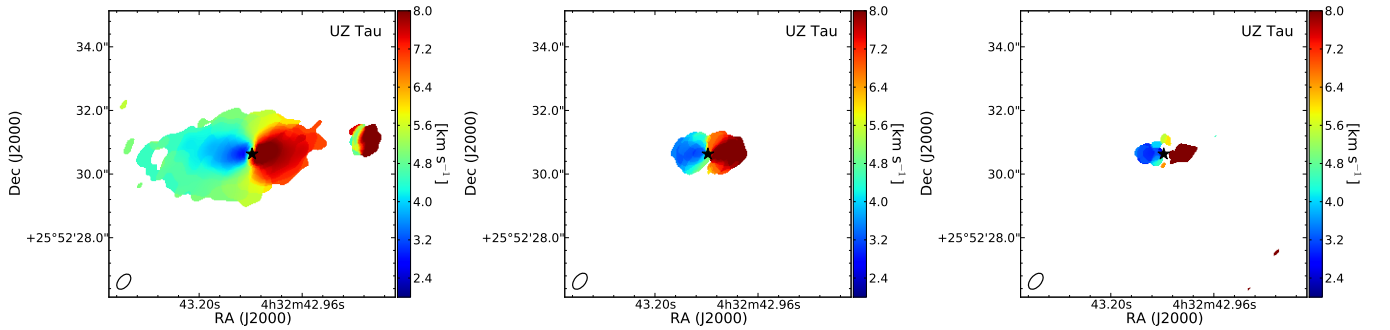


Figure 4. Maps of projected velocity centroids (moment 1) in ^{12}CO (left), ^{13}CO (middle) and C^{18}O (right) for UZ Tau E.

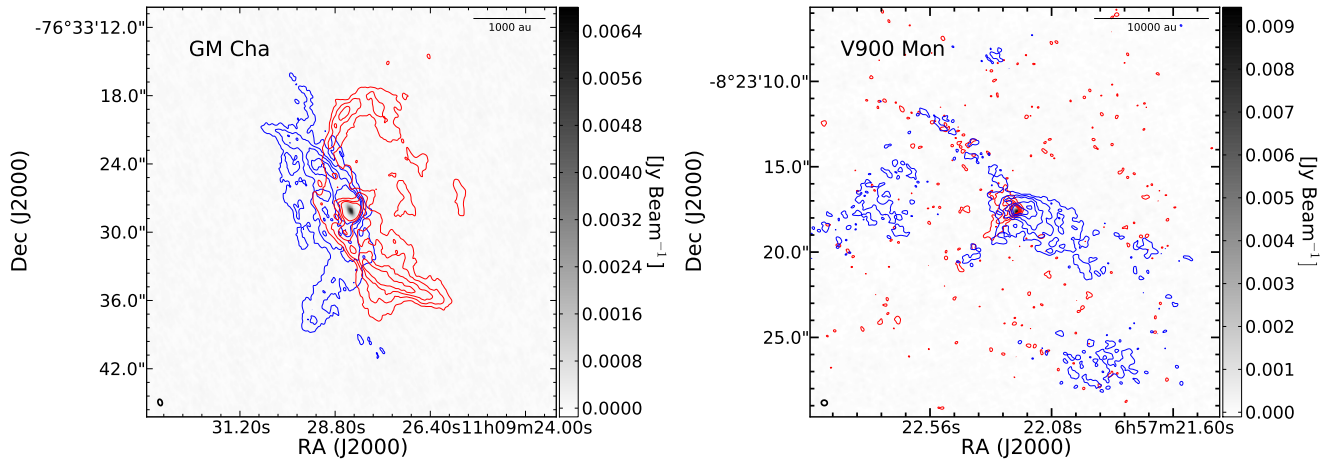


Figure 5. *Left:* Blue and red contours show the integrated intensity of the ^{12}CO blue- and red- shifted lobes of GM Cha (integrated between -10 and 4.5 km s^{-1} and 6.5 and 14.5 km s^{-1} respectively). Contour levels start at 3σ , increasing in steps of 2σ . The 1.3mm continuum image is shown in grayscale. *Right:* Same for V900 Mon. Emission for the blue and red lobes was integrated between 13.5 and 15.0 km s^{-1} and 15.5 and 18.0 km s^{-1} respectively. Contour levels start at 1.5σ , increasing in steps of 2σ .

Here we use the dust opacity of [Beckwith et al. \(1990\)](#), i.e. $\kappa_{1.3\text{mm}} \approx 0.022 \text{ cm}^2 \text{ g}^{-1}$, to compute dust masses from the fluxes and distances listed in Table 2. We list calculations assuming two dust temperatures, 20 K and 60 K. The former is the typical temperature of a passively heated protoplanetary disks ([Williams & Cieza 2011](#)) while the latter aims to represent more active, hotter, disks (see [Takami et al. 2019](#)). The derived disk dust masses are presented in Table 2. We also list the total disk mass (gas+dust) by assuming the standard gas-to-dust ratio of 100.

FUor sources in our sample have masses of solids which are at least one order of magnitude larger than those of the EXors, consistent with the trend reported in [Cieza et al. \(2018\)](#). The assumed temperature plays a significant role. Adopting a $3\times$ higher disk temperature yields a reservoir of solids ~ 3.6 times smaller in mass.

The dust mass estimate for UZ Tau E is consistent with the value derived by [Long et al. \(2018\)](#) using higher resolution data at similar frequency ($67 M_{\oplus}$ or $2.2 \times 10^{-4} M_{\odot}$). Assuming a 100:1 gas-to-dust ratio the total disk mass is $2.2 \times 10^{-2} M_{\odot}$. The total disk mass can also be obtained by comparing the $^{13}\text{CO}(2-1)$ to $\text{C}^{18}\text{O}(2-1)$ integrated line ratios to the grid of models from [Williams & Best \(2014\)](#). These models take into account basic CO chemistry (photodissociation and CO freeze-out) and provide an estimate of the total gas mass independent of the assumed gas-to-dust ratio. The comparison to the models yield a total gas mass of $3.2 \times 10^{-3} M_{\odot}$. Together with the dust mass estimated above, this implies a gas-to-dust ratio of 14, which is similar to the low ratios found around the EXor prototype EX Lupi and other Class II disks around Lupus ([Hales et al. 2018](#); [Ansdell et al. 2016](#); [Miotello et al. 2017](#)). This may be due to physical low amounts of gas, chemical conversion of CO into other species, or other physical processes ([Bosman et al. 2018](#); [Krijt et al. 2018](#); [Schwarz et al. 2018](#)).

We use radiative transfer codes in combination with MCMC methods to infer the UZ Tau E disk parameters from the continuum and line data independently. The dust and gas disks are modelled separately using the radiative transfer code RADMC-3D ([Dullemond et al. 2012](#)), adopting the standard tapered-edge model to describe the surface density profiles. See Appendix A for details on the modeling and MCMC procedure. These methods provide an alternative estimation of the disk dust and gas masses. We find that the masses of the dust and gas disks are $92.9_{-13.3}^{+3.6} M_{\oplus}$ ($2.8 \times 10^{-4} M_{\odot}$) and $7.8 \times 10^{-4} M_{\odot}$ respectively.

Both methods of deriving disk masses, from continuum and line emission, have caveats. The continuum radiative transfer modeling only accounts for a passive disk in hydrostatic equilibrium. While this is arguably a decent approximation to a protoplanetary disk, it may be far from the thermodynamical structure of actively accreting sources whose energy budget should include extra energy terms such as viscous heating, for example. This simplistic temperature structure also affects the molecular gas line modelling. The line modeling additionally suffers from uncertainties in CO isotopologue abundance ratios and a limited accounting of pho-

todissociation and freeze-out of the CO molecules. Bearing these caveats in mind, it is still possible to use these masses to gain a rough idea of the gas-to-dust mass ratio. This ratio would be approximately 2.8 for UZ Tau E, suggesting its disk has a higher concentration of dust, or a lower amount of gas, than the canonical assumption of a gas-to-dust mass of 100. The gas mass may have been reduced due to disk-binary interactions (see, for example, [Czekala et al. 2019](#)).

The total disk mass for V582 Aur, estimated assuming the dust emission is optically thin ($1055 M_{\oplus}$) and a gas-to-dust ratio of 100, is $0.3 M_{\odot}$, which is a factor of 7.5 larger than the estimate of [Ábrahám et al. \(2018\)](#). This discrepancy is mostly due to the new GAIA DR2 distance used in this work (2.5 kpc instead of 1.3 kpc), and cooler dust temperature (20 K instead of 30 K).

4.2. Disk Sizes

Figure 6 shows an updated version of Figure 6 in [Cieza et al. \(2018\)](#), in which disk sizes and total disk masses from the FU/EXor sample are compared to those of other protostellar and protoplanetary sources observed by ALMA ([Kóspál et al. 2017b](#); [Cieza et al. 2018](#); [Hales et al. 2018](#); [Kospal 2018](#); [Takami et al. 2019](#); [Cruz-Sáenz de Miera et al. 2019](#); [Pérez et al. 2020](#), and also this work). The properties of Class 0 and I protostellar disk candidates in Orion ([Tobin et al. 2020](#)) and the Class II disks in Lupus ([Ansdell et al. 2016](#)) are shown for comparison. We also compare the properties of eruptive sources to those of protostellar and protoplanetary disks in Ophiuchus from the Ophiuchus Disk Survey Employing ALMA (ODISEA, [Cieza et al. 2019](#)), which currently contains 12 Class I and 26 Class II sources with measured 1.3mm fluxes and resolved disk sizes.

The disk masses for the ODISEA sample are estimated assuming an optically thin dust continuum, a dust temperature of 20 K, and a gas-to-dust ratio of 100. Disk sizes are estimated from the deconvolved Gaussian FWHM/2 radius obtained from 2D Gaussian fits to the continuum images. [Cieza et al. \(2018\)](#) used the characteristic radius R_c (see Appendix A.1) as proxy for disk radius, while other authors have used the Gaussian 2σ radius or the curve-of-growth method to estimate the radius that contains a certain fraction of the total disk mass ([Bate 2018](#)) or a fraction of the total flux ([Tripathi et al. 2017](#); [Ansdell et al. 2018](#); [Trapman et al. 2019](#)). There are advantages and caveats on the ability of each method to measure the true sizes of circumstellar disks, which is beyond the purpose of this work (see discussions in e.g. [Tripathi et al. 2017](#); [Bate 2018](#); [Tobin et al. 2020](#)). We choose to use the deconvolved Gaussian FWHM/2 radius since it provides an homogeneous measure across the selected ALMA datasets. We find that the new eruptive sources presented here follow the same trend as the sample in [Cieza et al. \(2018\)](#), in which FUor disks are more massive than Class II sources of similar size. In contrast, the properties of the EXor disks are more consistent with those of Class II objects. As noted by [Tobin et al. \(2020\)](#), there does not seem to be a clear distinction in disk sizes between Class II in Lupus and the younger Class 0/I in Orion. Interestingly, we also find no difference when

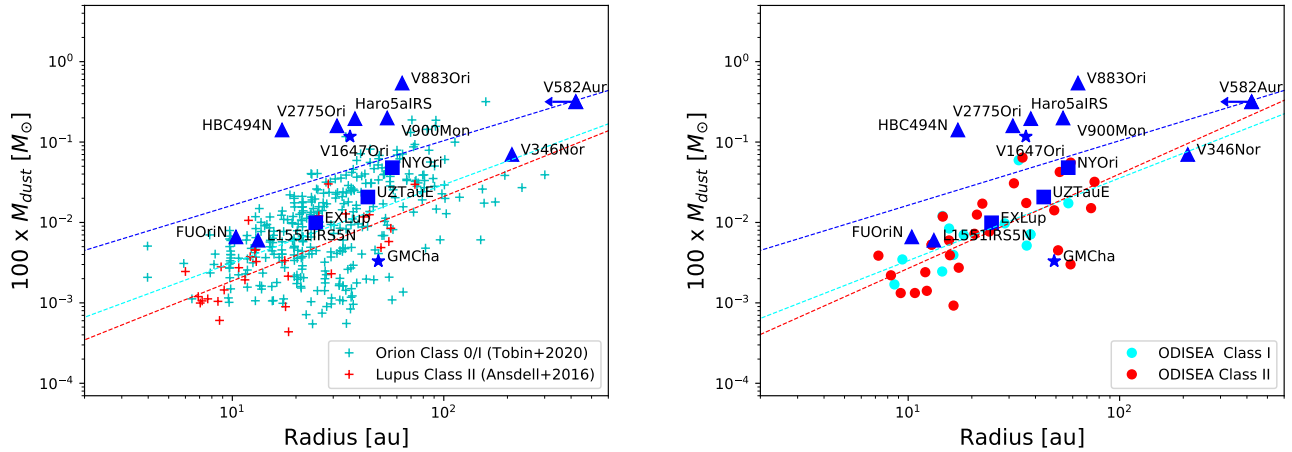


Figure 6. Relationship between disk mass and disk radius (FWHM/2) for FUor/EXor sources presented here (assuming a 20 K dust temperature) and in the literature. Squares are EXors, triangles are FUors, and objects with double FUor and EXor classification are marked with a star symbol. The disk size and mass for HBC494 correspond to the ones measured towards the brightest component of the binary, HBC494 North (Zurlo et al. in prep.). The horizontal arrow on V582 Aur denotes the disk radius is an upper limit. **Left panel:** Light blue crosses show the disk masses and radii (FWHM/2) for Class 0 and I protostellar disk candidates in Orion derived from 0.87 mm ALMA observations (Tobin et al. 2020). Red crosses show the disk masses and disk radii for Class II sources in Lupus from Ansdell et al. (2016). The dashed lines correspond to power law fits to the Class 0/I, Class II and FU/EXor data respectively. **Right panel:** Same as left panel, but now comparing the FU/EXor data to Class I and Class II sources in Ophiuchus from the ODISEA sample (Cieza et al. 2019).

comparing the Class II disk sizes to the Class I sources in Ophiuchus. This suggests that for a given disk size, the disks around FUor disks are brighter than disks of all protostellar classes. EXor disks, on the other hand, do not seem to be different from non-eruptive disks.

Two FUor disks deviate from this trend, FU Ori North and L1551 IRS 5 North, both of them are binary systems. The class prototype FU Ori North hosts the smallest disk of all eruptive targets (Pérez et al. 2020; Liu et al. 2019), which is part of a 210 au separation binary system. Both disks in the FU Ori system have similar 1.3mm sizes. Cruz-Sáenz de Miera et al. (2019) detected compact disks of similar sizes in another binary FUor-like system L1551 IRS 5. Recently Zurlo et al. (in prep.) resolved for the first time two binary components and their respective disks in the HBC 494 system which are also compact (<20 au). The small disk sizes found around binary FUor systems are consistent with observations of non-eruptive multiple systems in Orion. Tobin et al. (2020) found that multiple systems show the smallest (and faintest) distribution of disk sizes, which indicate that multiplicity has a significant impact on disk evolution. The disk sizes measured around binary FUor systems are consistent with simulations of stellar fly-bys in binary systems by Cuello et al. (2019). These simulations show that stellar encounters can deplete the disk outer regions and increase inner disk density, which can in turn enhance stellar accretion and explain the accretion outbursts of binary FUor systems.

The power law fits in Figure 6 can be inverted to estimate the relation of disk radius with disk mass. Tobin et al. (2020)

reports a power-law relation between disk radius and mass of $R \propto M^{0.30 \pm 0.03}$, which is similar to the power law scaling predicted by models of disk formation regulated by magnetic fields (which depend on magnetic field strength, ambipolar diffusion timescale and combined disk+stellar mass). The power law dependence for Class II in Lupus is steeper ($R \propto M^{0.46 \pm 0.09}$), closer to the square-root dependence predicted for optically thick disks. The fit to the FUor sample indicates that disk radii increase with mass as $R \propto M^{0.27 \pm 0.15}$. This is closer to the value of 0.3 found for Class 0/I protostars in Orion although with a larger uncertainty dominated by low number statistics. Increasing the FUor sample observed at sufficient high angular resolution will help improving the accuracy of the fit and allow a more consistent comparison with larger samples of Class 0/I and Class II sources. The size-luminosity relation has been studied intensively around over 200 Class II disks, for which a correlation between millimeter luminosity and dust disk size of $L \propto R^2$ has been well characterized (in agreement with the $R \propto M^{0.46}$ found for the Class II in Lupus, since millimeter luminosity is a proxy for mass; Tripathi et al. 2017; Andrews et al. 2018). Rosotti et al. (2019) showed that the size-luminosity relation can be explained by grain growth and radial drift, although it could also be related to disk initial conditions or to optical depth effects (Andrews et al. 2010; Andrews 2020, and references therein). Measuring the size-luminosity relation in episodically accreting disks, which are thought to be a common early phase of evolution of disks around low mass stars, may inform on the initial unruly dynamics of protoplanetary disks. If these active disks indeed reveal an earlier stage in disk evo-

lution, their size-luminosity relation allows for a more realistic description of the initial condition for later disk models, as an alternative for the classical 'steady state' start.

4.3. Gas Kinematics and Morphology

Complex kinematics can be the product of several types of dynamical interactions, such as flybys and binary interactions, outflows and winds, embedded planets and vortices, and the capture of cloud material. Several active sources are known binaries, such as UZ Tau E for example, and recent hydrodynamic models of tidal interactions have shown that tidal encounters have distinct kinematics signatures (Cuello et al. 2019) and that these encounters may be related to outbursting events. Interactions with an embedded sub-stellar perturber can excite kinematic perturbations (Perez et al. 2015) which could persist of large scales in the disk (Pérez et al. 2018). On the other hand, Dullemond et al. (2019) recently speculates that outbursting systems may be the result of cloudlet capture events, which do bear observational kinematics in the form of complex tail-like features in maps of line emission.

The molecular line data for the four sources observed have distinctive morphological features. GM Cha and V900 Mon $^{12}\text{CO}(2-1)$ integrated maps show the presence of wide-angle conical cavities. The presence of an $^{12}\text{CO}(3-2)$ outflow around GM Cha was first reported by Mottram et al. (2017) using APEX. The blue-shifted and red-shifted lobes are more clearly distinguished in GM Cha, while in V900 Mon the distinction is less clear. These morphologies are similar to the one observed in V883 Ori, HBC 494, V2775 Ori and V1647 Ori (Ruíz-Rodríguez et al. 2017a; Ruíz-Rodríguez et al. 2017b; Zurlo et al. 2017; Principe et al. 2018), in which opening cavities in $^{12}\text{CO}(2-1)$ are reported around all FUor candidates but not around the EXors. The observed emission is interpreted as the walls of a cavity that is carved out by a slow moving outflow, probably produced by material swept-up by a faster jet bow-shock (Frank et al. 2014). As the sources evolve from Class I to Class II, outflows carve out cavities that widen as the source ages (Arce & Sargent 2006), in a process that results in the dispersion of the remaining pre-stellar core. Combining ages derived using the L_{Bol} -age relation from Ladd et al. (1998), and the measured opening angles, Arce & Sargent (2006) found that sources with opening angles larger than ~ 150 degrees have ages of $\sim 10^6$ yr, closer to the typical ages of Class II stars.

The opening angles for the blue- and red-shifted lobes of GM Cha are both very similar ~ 120 degrees, measured at a distance of 1300 au). For V900 Mon the opening angle measured on the blue-shifted lobe is ~ 90 degrees. The opening angles of GM Cha are comparable to wide opening angles of 150 degrees measured around HBC 494 and V883 Ori (Ruíz-Rodríguez et al. 2017a; Ruíz-Rodríguez et al. 2017b). As noted by Takami et al. (2019), the opening angle of \sim V900 Mon is narrower than the one around these sources, but wider than the one measured around the eruptive Class 0 protostar V346 Nor (Kóspál et al. 2017b).

The presence of outflows in FUor sources (Ruíz-Rodríguez et al. 2017a; Ruíz-Rodríguez et al. 2017b; Kóspál et al. 2017b; Zurlo et al. 2017) and not around EXors suggests a distinction in the evolutionary stages between the two classes, with FUors closer to Class I sources. Nevertheless, EX Lupi and the ambiguously FUor/EXor classified V1647 Ori also have outflows (Principe et al. 2018; Hales et al. 2018). The outflows around these two EXors are fainter than the ones around FUors, therefore the distinction is more subtle and supports the idea of a continuous evolution from FUor to EXor, with EXors more evolved than FUors.

V582 Aur does not show a clear opening cavity but this may be due to the greater distance to the source. As a point of reference, V900 Mon is two times closer than V582 Aur but its outflow cavity walls were barely detected above the noise in our data. Another possibility is that the optical variability in V582 Aur is due to variable extinction and not accretion outbursts (Ábrahám et al. 2018). This would reinforce the picture that prominent cavity walls are carved during strong accretion outbursts. Deeper, higher resolution images of the more compact emission observed at the V582 Aur position could provide better understanding of its kinematics and relation to the FUor.

UZ Tau E, the only bona-fide EXor from our sample, is noticeably different from the FUors. It shows the clear Keplerian pattern of a Class II disk. This supports the evolutionary distinction between EXors and FUors. Cloud or envelope emission are most likely responsible to why Keplerian rotation is difficult to observe around most FUors. ^{12}CO and ^{13}CO are typically too contaminated by envelope emission, but a Keplerian disk is clearly seen in C^{18}O in V883 Ori (Cieza et al. 2016). It is possible that Keplerian rotation is not detected in some FUors simply because the observations are not deep enough, as C^{18}O is generally too faint for easy detection in other lower-mass stars (Ansdell et al. 2018). Ansdell et al. (2018) detected C^{18}O in the most massive disks in their sample, however most FUors are located 2-3 times further away than Lupus, with more extreme cases such as V900 Mon and V582 Aur that are 10 and 15 more distant than Lupus, respectively). Another possibility is that FUor disks are too perturbed and their kinematics distorted (due to the potential disk precession; Principe et al. 2018). High resolution observations of FU Ori reveal a rotation pattern distorted by complex kinematics (Pérez et al. 2020) possibly tracing binary interactions near the base of the outflow.

4.4. Triggering mechanisms

Observations of FUor objects suggest that the FUor phenomenon is an heterogenous process. Some systems harbour large, massive disks such as the ones detected around V883 Ori, V2775 Ori and V582 Aur. High resolution millimeter observations have also identified binary systems with compact, hot disks in each of the components (like FU Ori itself, HBC 494, and L1551 IRS 5).

Gravitational instability requires that the mass of the disk is at least 10% the mass of the central star in order to operate (see discussion in Cieza et al. 2018, and references therein),

and could possibly explain the outburst in the most massive disks. However high resolution observations do not show the signatures predicted by theoretical simulations of gravitationally unstable disks, as was demonstrated in the case of V883 Ori. High resolution ALMA images did not reveal the spiral or clumpy features predicted by GI simulations (Cieza et al. 2016). V582 Aur hosts the most massive disk our sample, yet being located 2.5 kpc away it was unresolved by our observations and therefore we are unable to test the GI scenario. Nevertheless, none of the massive FUor disks that have been resolved so far have show these signatures, which at least rules the possibility of GI operating in spatial scales compared to the spatial resolution of the observations. As pointed out by Cieza et al. (2018), the lack of large scale instabilities of fragmentation in these observations suggest that the outburst of these systems could support models that combine MRI and GI without fragmentation (e.g. Zhu et al. 2009b).

The outbursts in binary systems could be explained by perturbation of the accretion disk by a stellar companion. Bonnell & Bastien (1992) showed that binary perturbation can render the disk unstable and could possibly explain the triggering of FUor outbursts in multiple systems. As mentioned earlier, stellar fly-by scenario could also explain the compact sizes of the disks in binary systems as simulations by Cuello et al. (2019) show that an inclined prograde encounter can remove material from the outer disk and increase the inner disk density (which in turn can enhance the accretion).

Observations of EXors reveal disks that are similar to those observed around typical Class II sources, both in size and mass. The disks are not massive enough to satisfy the requirement for triggering gravitational instability. Most EXors resolved by ALMA so far, with the exception of UZ Tau E, are single star systems and therefore there is no clear connection between the EXor phenomenon and stellar multiplicity. As pointed out already by Cieza et al. (2018), the triggering mechanisms for EXor outburst is more likely associated to instabilities in the inner disks and/or interactions between the disk and planetary companions (Lodato & Clarke 2004).

5. CONCLUSION

We conducted a campaign to observe four young eruptive stellar systems with ALMA at $0''.4$ resolution. This sample represents 10% of known FUor/EXor objects in the non-exhaustive list of eruptive young stars from Audard et al. (2014), increasing the number of eruptive sources observed at sub-arcsecond resolution by 15%. We detected 1.3mm continuum emission in all four sources.

We found that the FUors have dust disks that are more massive than those around found around Class 0/I sources and Class II objects of similar size, making them more likely to become gravitationally unstable and trigger the outburst.

The EXor in our sample has a dust and gas disk that is well modeled with a passively irradiated disk in hydrostatic equilibrium, similar to those found in Class II sources.

We find that two of the three FUor objects show prominent outflows in molecular gas emission. While the FUor V900 Mon shows a distinct conical cavity similar to those of Class I objects, the source with unclear FU/EXor classification (GM Cha) has a wide-angle outflow similar to those found around a subset of FUor objects such as V883 Ori and HBC 494 (and FU Orionis itself; Hales et al. in prep.). Although the sample size remains small, the presence of outflow activity in FUors and not in EXors suggests that the two types of objects represent different evolutionary stages, with EXors more evolved than FUors.

These results highlight the importance of spectral line observations sensitive to various spatial scales for inferring the nature of eruptive sources, which seem to span from Class 0 to the early Class II stages of protostellar evolution. Observations targeting larger scale structure (>1000 au) are required, to determine the properties of outflows around FUors (and confirm their absence in EXors), while deeper continuum and $C^{18}O$ observations at few au resolution will measure the properties of their inner disks and help understand what drives this important early phase of star formation.

Software: Common Astronomy Software Applications (McMullin et al. 2007), RADMC-3D, (Dullemond et al. 2012), GALARIO, (Tazzari et al. 2017, 2018), EMCEE (Foreman-Mackey et al. 2013), Astropy (Astropy Collaboration et al. 2013)

ACKNOWLEDGMENTS

We thank the anonymous referee for a very constructive report. S.P acknowledges support from ANID-FONDECYT grant 1191934 and from the Joint Committee of ESO and the Government of Chile. A.Z. acknowledges support from the FONDECYT Iniciación en investigación project number 11190837. This paper makes use of the following ALMA data: ADS/JAO.ALMA#2017.1.01031.S. ALMA is a partnership of ESO (representing its member states), NSF (USA) and NINS (Japan), together with NRC (Canada) and NSC and ASIAA (Taiwan), in cooperation with the Republic of Chile. The Joint ALMA Observatory is operated by ESO, AUI/NRAO and NAOJ. The National Radio Astronomy Observatory is a facility of the National Science Foundation operated under cooperative agreement by Associated Universities, Inc. This work has made use of data from the European Space Agency (ESA) mission *Gaia* (<https://www.cosmos.esa.int/gaia>), processed by the *Gaia* Data Processing and Analysis Consortium (DPAC, <https://www.cosmos.esa.int/web/gaia/dpac/consortium>). Funding for the DPAC has been provided by national institutions, in particular the institutions participating in the *Gaia* Multilateral Agreement.

REFERENCES

Ábrahám, P., Kóspál, Á., Kun, M., et al. 2018, ApJ, 853, 28

Andrews, S. M., Wilner, D. J., Hughes, A. M., Qi, C., & Dullemond, C. P. 2010, ApJ, 723, 1241

- Andrews, S. M., Terrell, M., Tripathi, A., et al. 2018, *ApJ*, 865, 157
- Andrews, S. M. 2020, arXiv e-prints, arXiv:2001.05007
- Ansdell, M., Williams, J. P., van der Marel, N., et al. 2016, *ApJ*, 828, 46
- Ansdell, M., Williams, J. P., Trapman, L., et al. 2018, *ApJ*, 859, 21
- Arce, H. G., & Sargent, A. I. 2006, *ApJ*, 646, 1070
- Armitage, P. J., Livio, M., & Pringle, J. E. 2001, *MNRAS*, 324, 705
- Astropy Collaboration, Robitaille, T. P., Tollerud, E. J., et al. 2013, *A&A*, 558, AA33
- Audard, M., Abraham, P., Dunham, M. M., et al. 2014, *Protostars and Planets VI*, 387
- Bate, M. R. 2018, *MNRAS*, 475, 5618
- Beckwith, S. V. W., Sargent, A. I., Chini, R. S., & Guesten, R. 1990, *AJ*, 99, 924
- Bonnell, I., & Bastien, P. 1992, *ApJL*, 401, L31
- Bosman, A. D., Walsh, C., & van Dishoeck, E. F. 2018, *A&A*, 618, A182
- Calvet, N., Hartmann, L., & Kenyon, S. J. 1993, *The Astrophysical Journal*, 402, 623
- Chiang, E. I., & Goldreich, P. 1997, *ApJ*, 490, 368
- Cieza, L. A., Casassus, S., Tobin, J., et al. 2016, *Nature*, 535, 258
- Cieza, L. A., Ruíz-Rodríguez, D., Perez, S., et al. 2018, *MNRAS*, 474, 4347.
- Cieza, L. A., Ruíz-Rodríguez, D., Hales, A., et al. 2019, *MNRAS*, 482, 698
- Connelley, M. S., & Reipurth, B. 2018, *ApJ*, 861, 145
- Cruz-Sáenz de Miera, F., Kóspál, Á., Abraham, P., et al. 2019, arXiv e-prints, arXiv:1908.04649
- Cuello, N., Dipierro, G., Mentiplay, D., et al. 2019, *MNRAS*, 483, 4114
- Czekala, I., Chiang, E., Andrews, S. M., et al. 2019, *ApJ*, 883, 22
- Dewangan, L. K., Baug, T., Ojha, D. K., et al. 2018, *ApJ*, 864, 54
- Dullemond, C. P., Juhasz, A., Pohl, A., et al. 2012, *RADMC-3D: A multi-purpose radiative transfer tool*, ascl:1202.015
- Dullemond, C. P., Küffmeier, M., Goicovic, F., et al. 2019, *A&A*, 628, A20
- Dzib, S. A., Loinard, L., Ortiz-León, G. N., et al. 2018, *ApJ*, 867, 151
- Evans, N. J., II, Dunham, M. M., Jørgensen, J. K., et al. 2009, *ApJS*, 181, 321-350
- Foreman-Mackey, D., Hogg, D. W., Lang, D., & Goodman, J. 2013, *PASP*, 125, 306
- Frank, A., Ray, T. P., Cabrit, S., et al. 2014, *Protostars and Planets VI*, 451
- Gaia Collaboration, Brown, A. G. A., Vallenari, A., et al. 2018, *A&A*, 616, A1
- Gonzalez C., Hales, A. S., Cieza, L. A. et al. in preparation
- Grinin, V. P., Semenov, A. O., Barsunova, O. Y., et al. 2019, *Astrophysics*, 62, 41
- Hales, A. S., Corder, S. A., Dent, W. R. D., et al. 2015, *ApJ*, 812, 134
- Hales, A. S., Pérez, S., Saito, M., et al. 2018, *ApJ*, 859, 111
- Hales, A. S., Williams, J. P., Cieza, L. A. et al., in preparation
- Hartmann, L., & Kenyon, S. J. 1985, *ApJ*, 299, 462
- Hartmann, L., & Kenyon, S. J. 1996, *ARA&A*, 34, 207
- Hartmann, L. 2008, *Accretion Processes in Star Formation*, Cambridge, UK: Cambridge University Press, 2008,
- Hartmann, L., Herczeg, G., & Calvet, N. 2016, *ARA&A*, 54, 135
- Herbig, G. H. 1966, *Vistas in Astronomy*, 8, 109
- Herbig, G. H., & Harlan, E. A. 1971, *Information Bulletin on Variable Stars*, 543, 1
- Hildebrand, R. H. 1983, *QJRAS*, 24, 267
- Huang, J., Andrews, S. M., Dullemond, C. P., et al. 2018, *ApJL*, 869, L42
- Hubbard, A. 2017, *MNRAS*, 465, 1910
- Jensen, E. L. N., Dhital, S., Stassun, K. G., et al. 2007, *AJ*, 134, 241
- Jones, T. J., Hyland, A. R., Harvey, P. M., et al. 1985, *AJ*, 90, 1191
- Johnstone, D., Herczeg, G. J., Mairs, S., et al. 2018, *The Astrophysical Journal*, 854, 31
- Kenyon, S. J., Hartmann, L. W., Strom, K. M., et al. 1990, *AJ*, 99, 869
- Kóspál, Á., Abraham, P., Csengeri, T., et al. 2017, *ApJ*, 843, 45
- Kospal, A. 2018, *Take a Closer Look*, 15-19 October, 2018 in ESO-HQ, Garching b. Munchen, Germany. Online at <http://www.eso.org/sci/meetings/2018/tcl2018.html>, tcl2018, id.87
- Krijt, S., Schwarz, K. R., Bergin, E. A., et al. 2018, *ApJ*, 864, 78
- Kun, M., Szegedi-Elek, E., & Reipurth, B. 2017, *MNRAS*, 468, 2325
- Ladd, E. F., Fuller, G. A., & Deane, J. R. 1998, *ApJ*, 495, 871
- Liu, H. B., Dunham, M. M., Pascucci, I., et al. 2018, *A&A*, 612, A54
- Liu, H. B., Mérand, A., Green, J. D., et al. 2019, *ApJ*, 884, 97
- Lodato, G., & Clarke, C. J. 2004, *MNRAS*, 353, 841
- Long, F., Pinilla, P., Herczeg, G. J., et al. 2018, *ApJ*, 869, 17
- Lorenzetti, D., Giannini, T., Larionov, V. M., et al. 2007, *ApJ*, 665, 1182
- Lynden-Bell, D., & Pringle, J. E. 1974, *MNRAS*, 168, 603
- Manara, C. F., Tazzari, M., Long, F., et al. 2019, *A&A*, 628, A95
- Marino, S., Wyatt, M. C., Panić, O., et al. 2017, *MNRAS*, 465, 2595
- Moody, M. S. L., & Stahler, S. W. 2017, *A&A*, 600, A133
- Mathieu, R. D., Martin, E. L., & Magazzu, A. 1996, *American Astronomical Society Meeting Abstracts #188* 188, 60.05
- Mattila, K., Liljeström, T., & Toriseva, M. 1989, *European Southern Observatory Conference and Workshop Proceedings*, 153

- McMullin, J. P., Waters, B., Schiebel, D., Young, W., & Golap, K. 2007, *Astronomical Data Analysis Software and Systems XVI*, 376, 127
- Miotello, A., van Dishoeck, E. F., Williams, J. P., et al. 2017, *A&A*, 599, A113
- Mottram, J. C., van Dishoeck, E. F., Kristensen, L. E., et al. 2017, *A&A*, 600, A99
- Perez, S., Dunhill, A., Casassus, S., et al. 2015, *ApJL*, 811, L5
- Pérez, S., Casassus, S., & Benítez-Llambay, P. 2018, *MNRAS*, 480, L12
- Pérez, S., Hales, A., Liu, H. B., et al. 2020, *ApJ*, 889, 59
- Persi, P., Tapia, M., Gómez, M., et al. 2007, *AJ*, 133, 1690
- Pinte, C., Dent, W. R. F., Ménard, F., et al. 2016, *ApJ*, 816, 25
- Prato, L., Simon, M., Mazeh, T., et al. 2002, *ApJL*, 579, L99
- Principe, D. A., Cieza, L., Hales, A., et al. 2018, *MNRAS*, 473, 879
- Reipurth, B., Aspin, C., & Herbig, G. H. 2012, *ApJ*, 748, L5
- Reipurth, B., & Aspin, C. 2010, *Evolution of Cosmic Objects Through Their Physical Activity*, 19
- Rosotti, G. P., Booth, R. A., Tazzari, M., et al. 2019, *MNRAS*, 486, L63
- Ruíz-Rodríguez, D., Cieza, L. A., Williams, J. P., et al. 2017, *MNRAS*, 466, 3519
- Ruíz-Rodríguez, D., Cieza, L. A., Williams, J. P., et al. 2017, *MNRAS*, 468, 3266.
- Safron, E. J., Fischer, W. J., Megeath, S. T., et al. 2015, *ApJL*, 800, L5
- Samus, N. 2009, *Central Bureau Electronic Telegrams* 1896, 1
- Schwarz, K. R., Bergin, E. A., Cleeves, L. I., et al. 2018, *ApJ*, 856, 85
- Segura-Cox, D. M., Looney, L. W., Tobin, J. J., et al. 2018, *ApJ*, 866, 161
- Tobin, J. J., Sheehan, P., Megeath, S. T., et al. 2020, *arXiv e-prints*, arXiv:2001.04468
- Semkov, E. H., Peneva, S. P., Munari, U., et al. 2013, *A&A*, 556, A60
- Sheehan, P. D., Wu, Y.-L., Eisner, J. A., et al. 2019, *The Astrophysical Journal*, 874, 136
- Simon, M., Dutrey, A., & Guilloteau, S. 2000, *ApJ*, 545, 1034
- Sipos, N., Ábrahám, P., Acosta-Pulido, J., et al. 2009, *A&A*, 507, 881
- Takami, M., Fu, G., Liu, H. B., et al. 2018, *The Astrophysical Journal*, 864, 20
- Takami, M., Chen, T.-S., Liu, H. B., et al. 2019, *ApJ*, 884, 146
- Tazzari, M., Beaujean, F., & Testi, L. 2017, *galario: Gpu Accelerated Library for Analyzing Radio Interferometer Observations*, ascl:1710.022
- Tazzari, M., Beaujean, F., & Testi, L. 2018, *Monthly Notices of the Royal Astronomical Society*, 476, 4527
- Thommes, J., Reipurth, B., Aspin, C., et al. 2011, *Central Bureau Electronic Telegrams* 2795, 1
- Trapman, L., Facchini, S., Hogerheijde, M. R., et al. 2019, *A&A*, 629, A79
- Tripathi, A., Andrews, S. M., Birnstiel, T., et al. 2017, *ApJ*, 845, 44
- Tripathi, A., Andrews, S. M., Birnstiel, T., et al. 2018, *ApJ*, 861, 64
- Vorobyov, E. I., & Basu, S. 2015, *ApJ*, 805, 115
- Williams, J. P., & Cieza, L. A. 2011, *ARA&A*, 49, 67
- Williams, J. P., & Best, W. M. J. 2014, *ApJ*, 788, 59
- Wilson, T. L., & Rood, R. 1994, *ARA&A*, 32, 191
- Zhu, Z., Espaillat, C., Hinkle, K., et al. 2009, *ApJL*, 694, L64
- Zhu, Z., Hartmann, L., Gammie, C., et al. 2009, *ApJ*, 701, 620
- Zsidi, G., Ábrahám, P., Acosta-Pulido, J. A., et al. 2019, *ApJ*, 873, 130
- Zurlo, A., Cieza, L. A., Williams, J. P., et al. 2017, *MNRAS*, 465, 834
- Zurlo, A., Cieza, L. A., Williams, J. P., et al. in preparation

APPENDIX

A. RADIATIVE TRANSFER MODELING OF UZ TAU E

A.1. *Dust continuum model*

The millimeter continuum disk around UZ Tau E has been studied intensively in previous works: [Tripathi et al. \(2018\)](#) using CARMA, [Long et al. \(2018\)](#) and [Manara et al. \(2019\)](#) using higher resolution ALMA data. To compare the properties (mainly size and perhaps the mass) of the dust disk around UZ Tau E to the ones of other eruptive sources studied by our group, we modelled the continuum emission with a simple passively heated disk. The model assumes a power-law for the surface density profile with an exponential taper beyond a characteristic radius. The exact formulation of the model and the radiative transfer calculation are described in [Cieza et al. \(2018\)](#), [Hales et al. \(2018\)](#) and [Pérez et al. \(2020\)](#) –we refer the readers to these works for a detailed description of the radiative transfer modelling.

The disk model is described by 5 free parameters: the dust mass M_{disk} , the slope of the surface density power law γ , the characteristic radius R_c , the scale height at 100 au H_{100} and the flaring index Ψ . The flux emerging from the parametric disk model is computed using the radiative transfer code RADMC-3D (version 0.41, [Dullemond et al. 2012](#)).

The stellar parameters that we adopt for UZ Tau E are: an effective stellar temperature of 3574 K and a luminosity of $0.35 L_{\odot}$ ([Long et al. 2018](#)). The assumed distribution of dust grains and their optical properties are the same as the ones adopted in our previous works (the dust absorption opacity at 1.3 mm is $\kappa_{\text{abs}} = 0.022 \text{ cm}^2 \text{ g}^{-1}$). The inclination angle i and PA of the model are fixed to the values derived by [Long et al. \(2018\)](#) from higher resolution images.

The EMCEE MCMC algorithm ([Foreman-Mackey et al. 2013](#)) was used to sample the posterior distributions of each parameter. We run RT models with 240 walkers for 1000 iterations. The resulting posteriors are shown in Fig. 10. We note that since the model is a passive disk (it neglects, for example, viscous heating), the derived temperatures serve only as a crude approximation for the dust temperature. Nevertheless, the best-fit (maximum likelihood set of parameters) model allows to obtain a crude estimate of the size and bulk mass of the disk. The 1.3 mm observations of UZ Tau E can thus be described by a disk profile with characteristic radii of 61 au and total dust mass of $92.9 M_{\oplus}$ ($2.8 \times 10^{-4} M_{\odot}$). The slope of the surface density distribution is 0.8, similar to those of T Tauri stars ([Andrews et al. 2010](#)). See corner Figure 10 for parameter uncertainties. The parameters' posterior distributions show that there could be some degeneracies in our modelling. We think this could be due to underlying structures not accounted for in our simple model. Higher resolution data, and a more complete model that includes viscous heating, would be required to describe the UZ Tau E disk in detail.

B. ^{13}CO AND C^{18}O GAS MODEL

In this section we focus in modelling of the ^{13}CO and C^{18}O gas emission detected by our ALMA observations. We use the PDSPY code from [Sheehan et al. \(2019\)](#) to generate synthetic molecular line emission channel maps from a model of a Keplerian-rotating, passively irradiated disk in hydrostatic equilibrium. The models are then used to fit the ^{13}CO and C^{18}O data simultaneously using a Markov Chain Monte Carlo (MCMC) routine. The code is described in detail in [Sheehan et al. \(2019\)](#), and it uses RADMC-3D to ray-trace the density and temperature structure, and GALARIO for fast sampling of the visibilities from the synthetic channel maps generated by RADMC-3D ([Tazzari et al. 2018](#)). The model visibilities are then provided as input to an MCMC routine that makes use of the EMCEE code [Foreman-Mackey et al. \(2013\)](#) to compare the synthetic observations with our data.

The model adopted here includes 13 parameters: total disk mass M_{disk} , combined stellar mass M_* , disk characteristic radius R_{disk} , disk inner radius R_{in} , T_0 , a_{turb} , position angle PA, q , system velocity v_{sys} (LSRK), and offset from the phase center x_0 and y_0 . The dynamical mass of the central object M_* is fitted as part of our model, assuming the distance of 131.2 ± 1.7 pc ([Gaia Collaboration et al. 2018](#)). The disk is assumed to be vertically isothermal, with a power-law radial dependence of the temperature given by

$$T(r) = T_0 \left(\frac{r}{1 \text{ au}} \right)^{-q}, \quad (\text{B1})$$

where T_0 corresponds to the temperature at 1 au, and q is the radial exponent for the temperature dependence. The surface density profile of the disk is given by Equation A1, with the vertical structure determined by using the vertically isothermal temperature (Equation B4) to solve for hydrostatic equilibrium. Following [Czekala et al. \(2019\)](#) we fixed q to 0.5, the surface density power law exponent γ to 1.0 and the inclination angle of the disk to 56.16° . M_{disk} is the total gas mass. The abundance of ^{12}CO relative to H_2 was set to 10^{-4} and assumed constant throughout the disk. We adopt the canonical values for the ^{13}CO and C^{18}O isotopologue ratios with respect to ^{12}CO (77 and 550, respectively; [Wilson & Rood 1994](#)).

Each run was started with 100 walkers and were run for ~ 2500 steps. Detailed description of the MCMC fitting procedure can be found in Appendix A1 of [Sheehan et al. \(2019\)](#). In Table 4 we show the best fit parameters obtained computing the median value of the MCMC samples after removing the burn-in steps. The triangle plots of the posterior probability distribution function

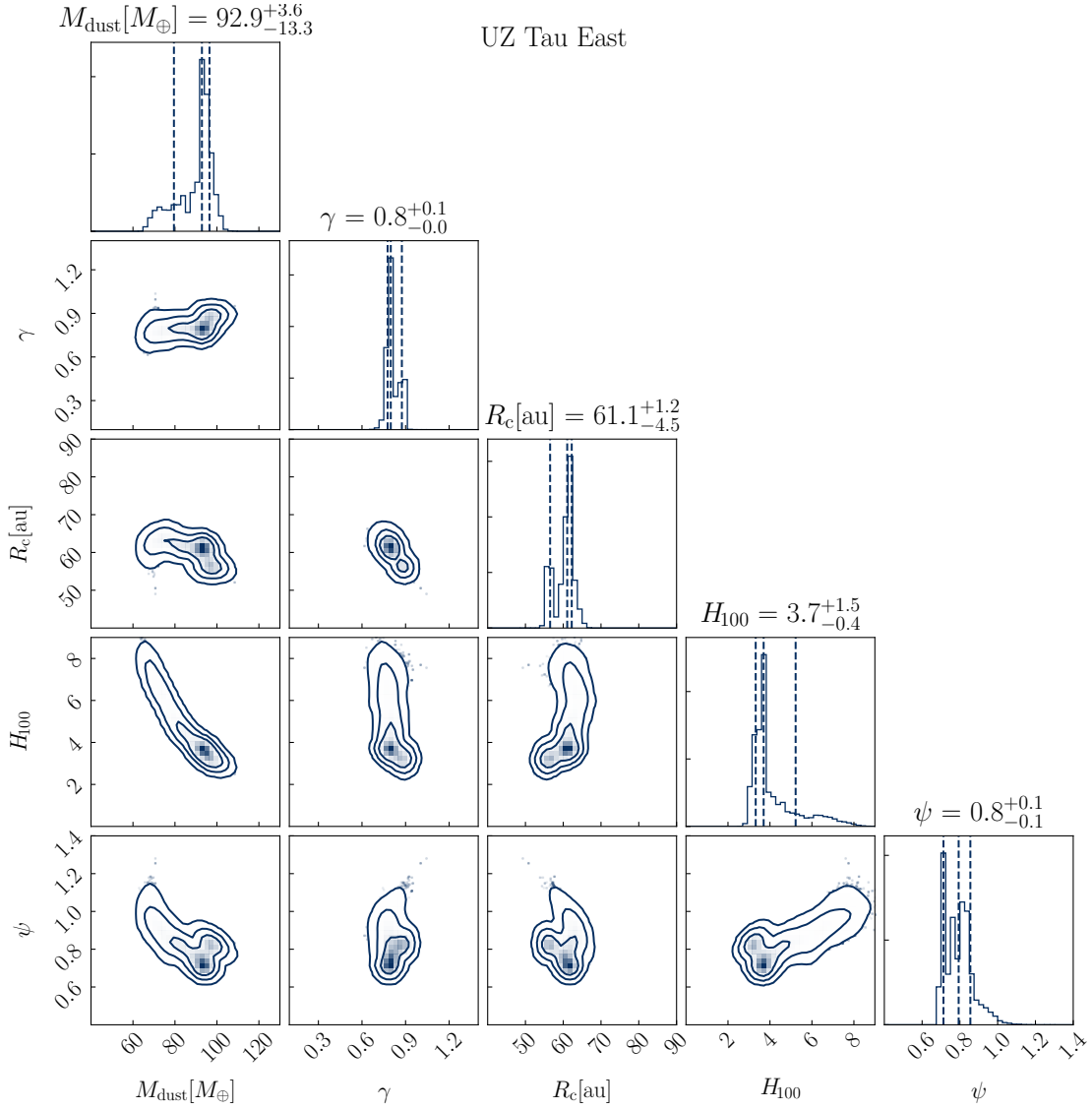


Figure 7. Triangle plots of the posterior probability distribution function for the different model parameters.

from the MCMC fitting process are shown in Figure 10. The uncertainty for each variable parameter are estimated by considering the range around the median value that contains 68% of the walker positions (after removing the burn-in steps).

We find a combined stellar mass for M1+M2 of $1.25 \pm 0.009 M_{\odot}$ add 1% uncertainty on distance in quadrature., comparable to the $1.3 \pm 0.08 M_{\odot}$ derived using ^{12}CO from the IRAM Plateau de Bure interferometer (Simon et al. 2000) and to the $1.23 \pm 0.12 M_{\odot}$ derived by Czekala et al. (2019) using ALMA data at 0.6-0.7'' resolution of the same CO isotopologues in our data. We derive a total disk mass of $0.00078 \pm 0.00003 M_{\odot}$.

C. CHANNEL MAPS

Figures 11, 12 and 13 show the channel maps for V582 Aur in $^{12}\text{CO}(2-1)$, $^{13}\text{CO}(2-1)$ and $\text{C}^{18}\text{O}(2-1)$ respectively. Figure 14 shows the moment 0 maps for $^{13}\text{CO}(2-1)$ and $\text{C}^{18}\text{O}(2-1)$ computed in the same velocity ranges as Figure 2.

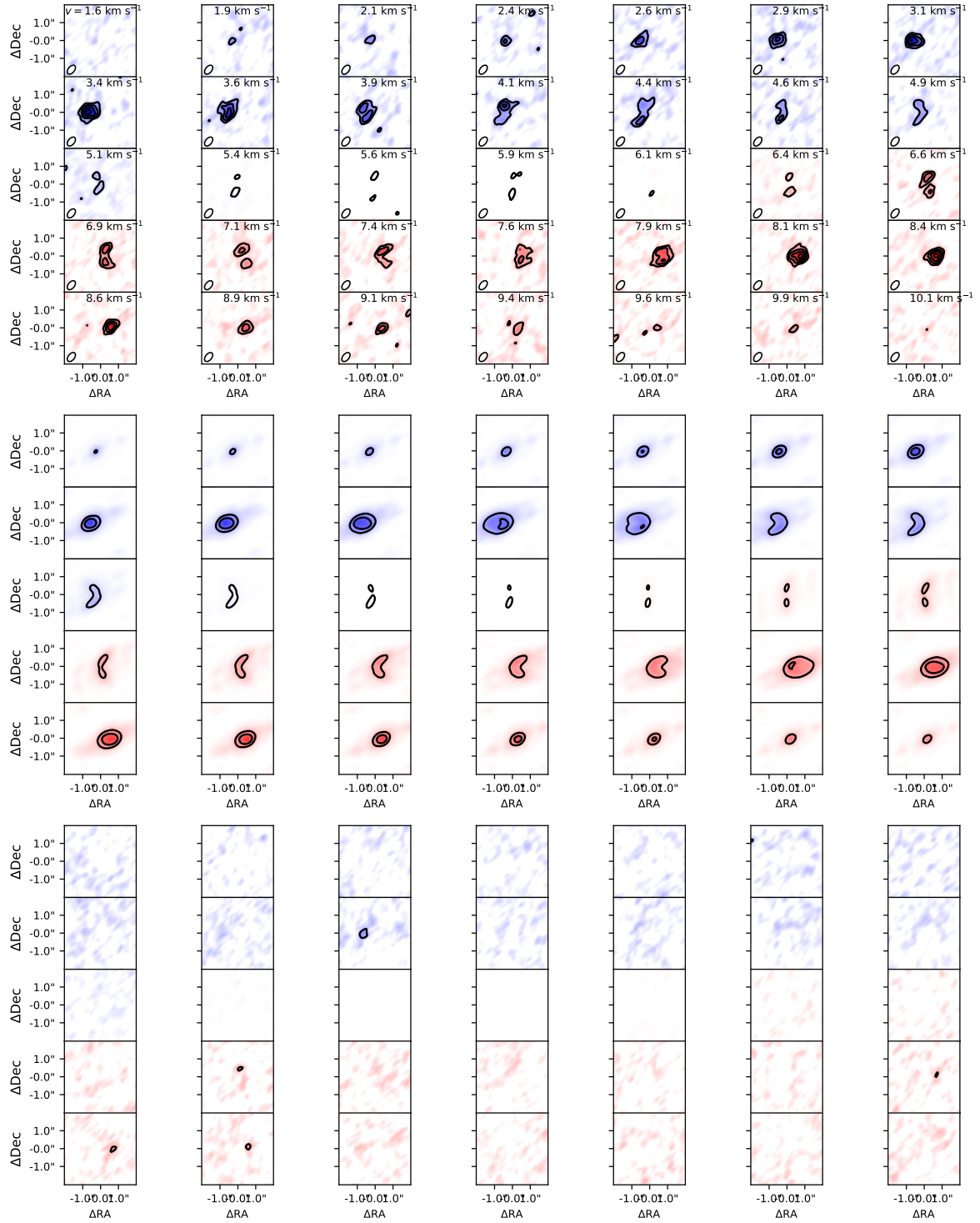


Figure 8. ^{13}CO channel maps for UZ Tau E (top), best-fit disk model (middle) and residuals (bottom). Contour levels start at 3.5σ , with increments of 3σ .

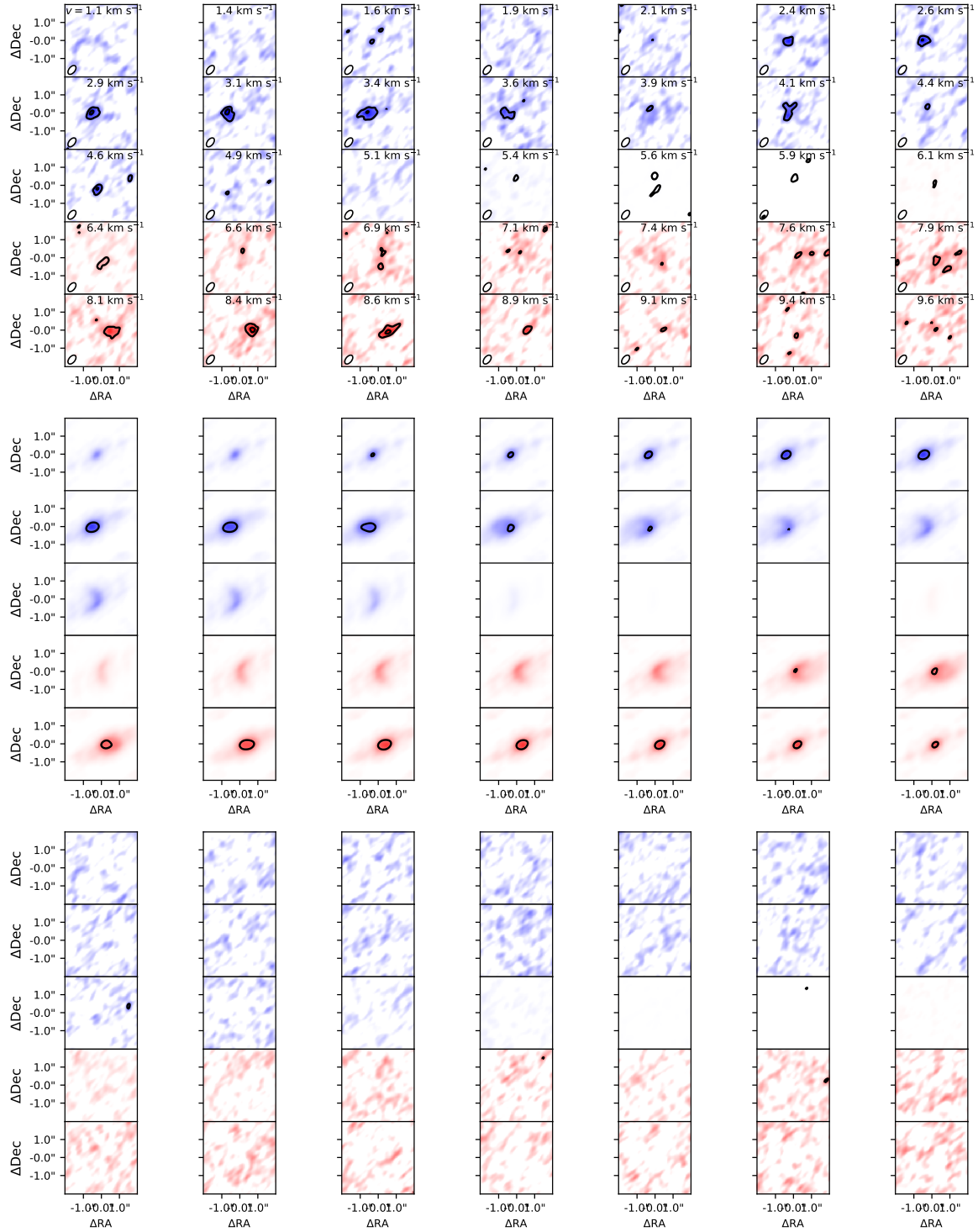


Figure 9. $C^{18}O$ channel maps for UZ Tau E (top), best-fit disk model (middle) and residuals (bottom).

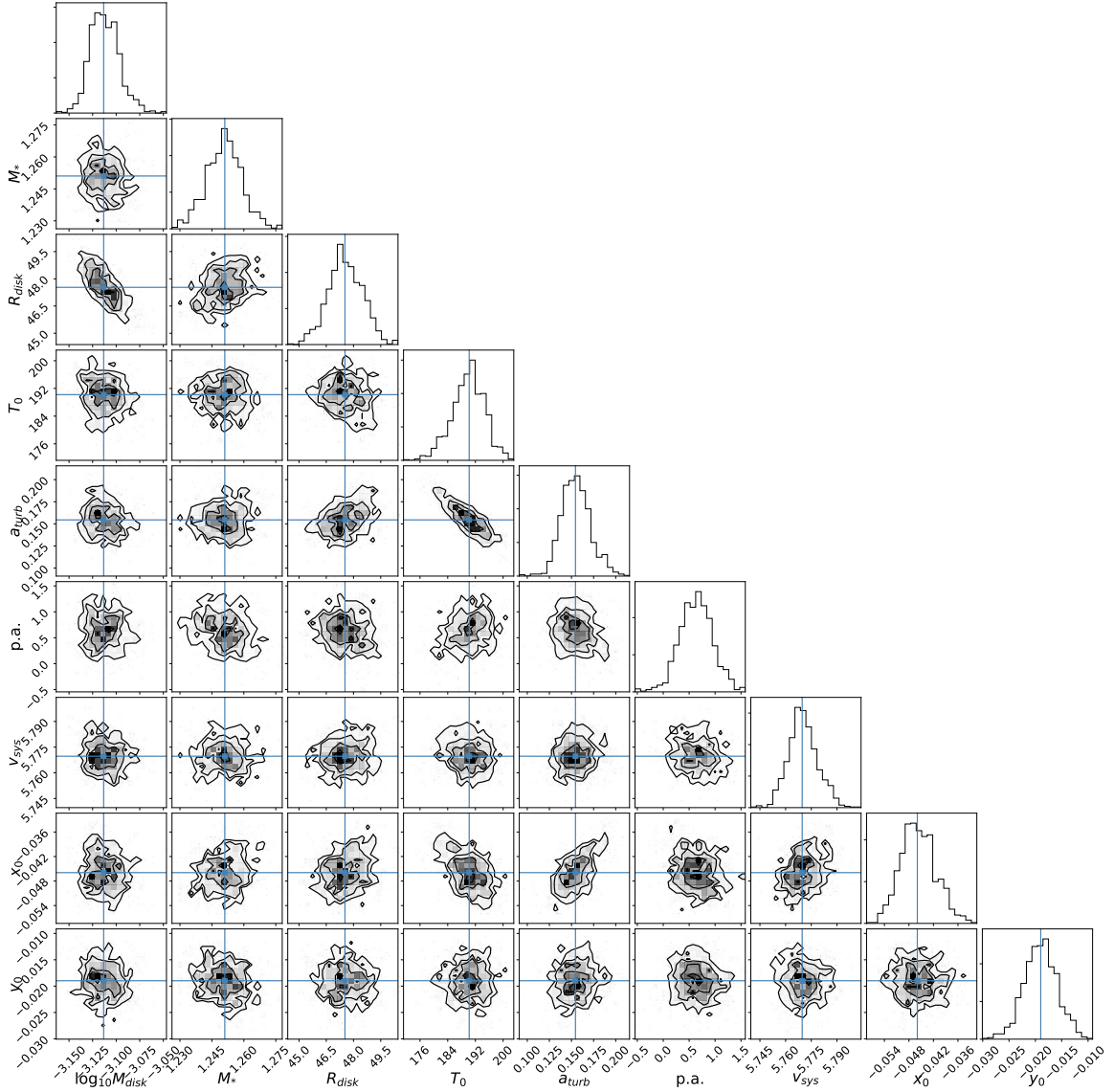


Figure 10. Triangle plots of the posterior probability distribution function for the different model parameters.

Table 4. Best-fit model parameters for UZ Tau E

γ	i	M_{disk}	M_*	R_{disk}	R_{in}	T_0	a_{turb}	pa	q	v_{sys}	x_0	y_0
	[$^\circ$]	[M_\odot]	[M_\odot]	[au]	[au]	[K]	[km s^{-1}]	[$^\circ$]		[km s^{-1}]	[mas]	[mas]
1.0^α	56.15^α	0.00078 ± 0.00003	1.253 ± 0.009	48.1 ± 1.1	1.0^α	187.3 ± 4.6	0.171 ± 0.016	1.1 ± 0.3	0.5^α	5.77 ± 0.01	-0.051 ± 0.004	-0.013 ± 0.003

NOTE— $^\alpha$ Parameter is fixed.

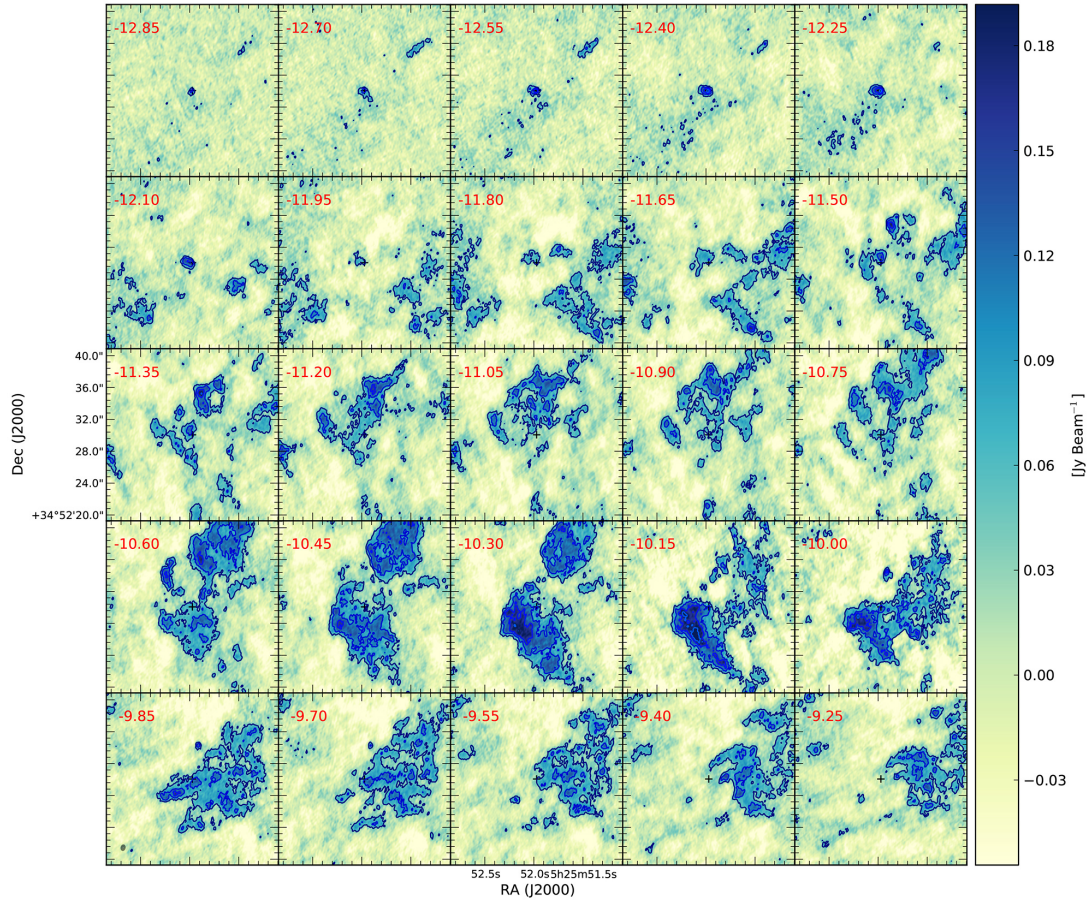


Figure 11. ^{12}CO channel maps for V582 Aur. Contour levels start at 3σ , increasing in steps of 3σ ($\sigma=16 \text{ mJy beam}^{-1}$). The position of the star is marked with a cross. The beam is represented by a gray ellipse in the bottom left corner of the bottom left panel.

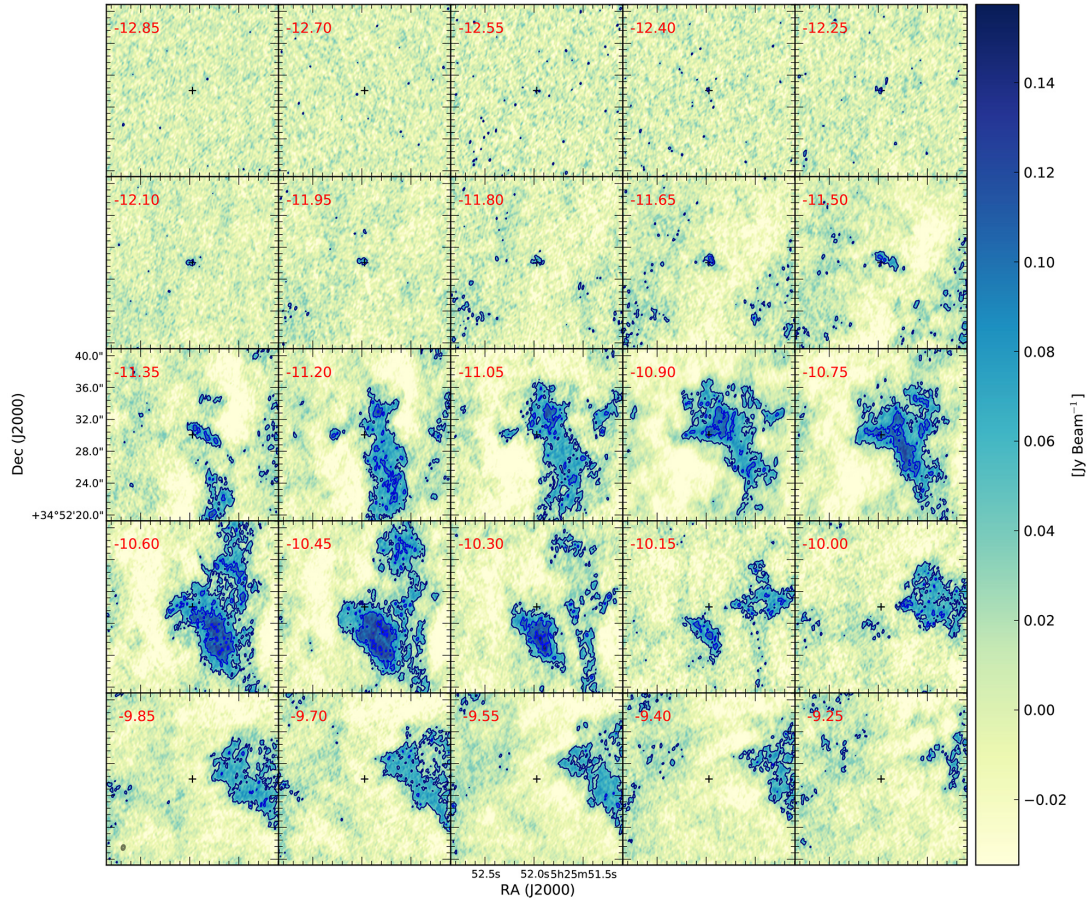


Figure 12. ^{13}CO channel maps for V582 Aur. Contour levels start at 3σ , increasing in steps of 3σ ($\sigma=17 \text{ mJy beam}^{-1}$). The position of the star is marked with a cross. The beam is represented by a gray ellipse in the bottom left corner of the bottom left panel.

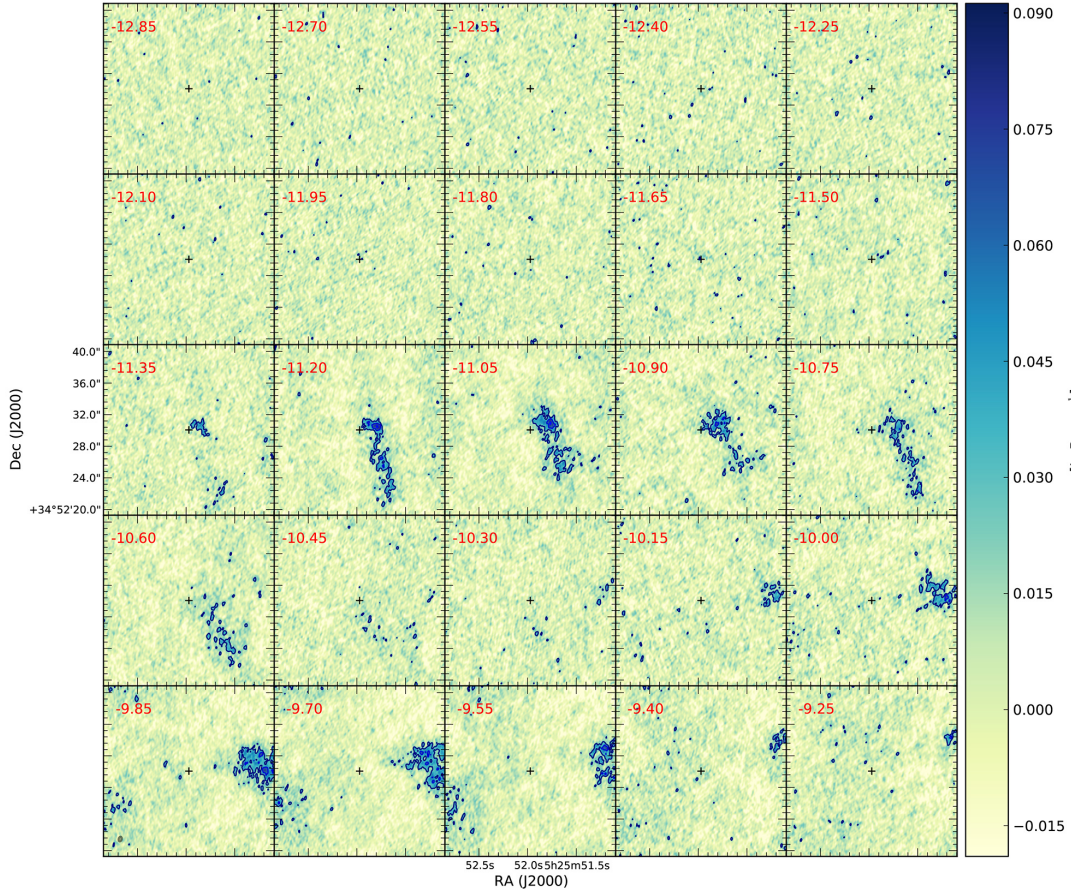


Figure 13. C^{18}O channel maps for V582 Aur. Contour levels start at 3σ , increasing in steps of 3σ ($\sigma=10 \text{ mJy beam}^{-1}$). The position of the star is marked with a cross. The beam is represented by a gray ellipse in the bottom left corner of the bottom left panel.

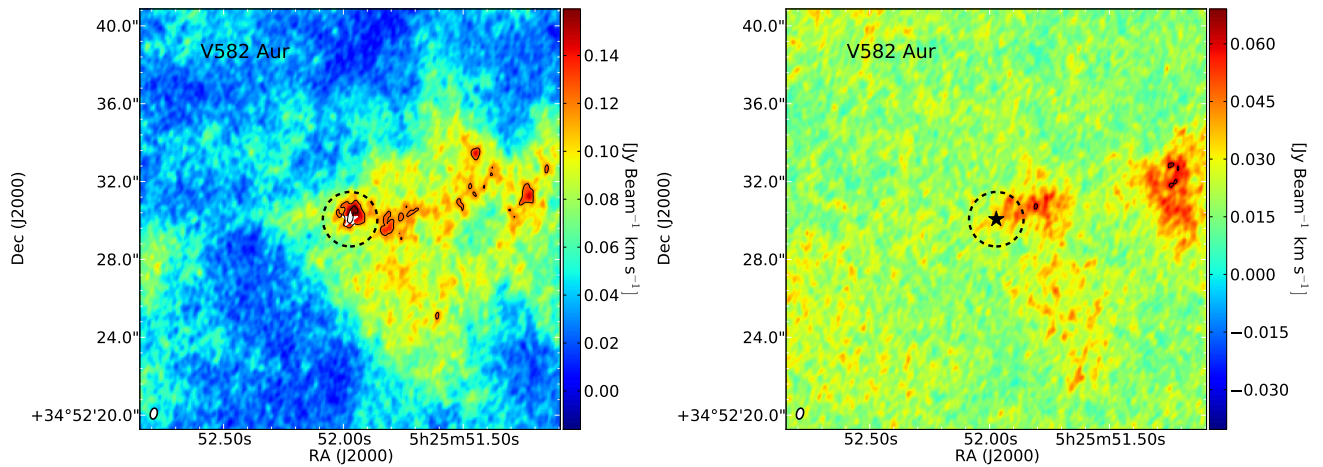


Figure 14. $^{13}\text{CO}(2-1)$ and $\text{C}^{18}\text{O}(2-1)$ moment 0 maps for V582 Aur (left and right panels, respectively). Contour levels start at 3σ , increasing in steps of 1σ . The dashed circles shows the region used to compute the integrated line emissions listed in Table 3. The peak position of the continuum is shown with a star symbol. The moment 0 maps were computed in the same velocity ranges as Figure 2.